

How does a collapsing star look?

Hiroataka Yoshino⁽¹⁾, Kazuma Takahashi⁽²⁾, and Ken-ichi Nakao^{(2),(3)}

⁽¹⁾*Advanced Mathematical Institute,*

Osaka City University, Osaka 558-8585 Japan

⁽²⁾*Department of Mathematics and Physics, Graduate School of Science,*

Osaka City University, Osaka 558-8585, Japan and

⁽³⁾*Nambu Yoichiro Institute of Theoretical and Experimental Physics (NITEP),*

Osaka City University, Osaka 558-8585, Japan

(Dated: Submitted 23 August 2019; published 28 October 2019)

Abstract

Time evolution of an optical image of a pressureless star under gravitational collapse is studied in the geometric optics approximation. The star surface is assumed to emit radiation obeying Lambert's cosine law but with an arbitrary spectral intensity in the comoving frame. We develop a formalism for predicting observable quantities by photon counting and by radiometry, in particular, spectral photon flux and spectral radiant flux. Then, this method is applied to the two cases: One is monochromatic radiation, and the other is blackbody radiation. The two kinds of spectral flux are calculated numerically for each case. It is reconfirmed that the redshift factor remains finite and the star becomes gradually invisible due to decay of the photon flux. We also develop an approximate method to present analytic formulas that describe the late time behavior. A possible connection of our study to observation of high-energy neutrinos is briefly discussed.

PACS numbers: 04.70.Bw, 04.20.-q, 97.60.Bw, 97.60.Lf

I. INTRODUCTION

We are now in the era to observe phenomena caused by strong gravity. The great discoveries of gravitational waves have been made at advanced LIGO and Virgo detectors ([1] for the first one), and it is widely believed that they were from mergers of binary black holes/neutron stars. Also, the Event Horizon Telescope Collaboration has succeeded in taking the observational image of a shadow caused by the massive object at the center of the galaxy M87, which is supposed to be a supermassive black hole,¹ through radio observations [2]. The primary factor to determine the shape of black hole shadows are circular orbits of photons on the photon spheres or the photon surfaces [4, 5] or its extension, the fundamental photon orbits [6]. Roughly speaking, they are typically located at positions whose distance from the event horizon is order of the black hole mass, $\sim M$ (in the unit where the Newtonian constant of gravitation becomes $G_N = 1$).

The black hole is defined as a complement of the causal past of the future null infinity or, in other words, a spacetime region from which no information can escape to infinity. This definition implies that a black hole and its any physical influences must not exist in the view of any observer staying outside the black hole. Therefore, as commented in Ref. [7], “*observational proof for black holes is, by definition, impossible to obtain.*”

Black holes in our Universe will form through gravitational collapse of massive objects. As is well known, collapsing massive objects form black holes in the infinitely far future in the view of any distant observer: The distant observers will see objects collapsing forever, even though they will form black holes. One of the very nontrivial *observable* predictions made by general relativity must not be the formation of black holes but is the process in which the spacetime geometry of the domain around a collapsing object asymptotically approaches the one described by the metric of the Kerr-Newman family. In this paper, we consider electromagnetic signals from a dynamically collapsing object. To be specific, consider a star under the gravitational collapse that emits radiation from its surface. At a distant place, an observer looks at the collapse with photons, e.g., by a telescope. Then, what kind of an image does the observer see, and how does it change as time goes on? We would like to give an answer to these questions in the framework of general relativity. The

¹ See also [3] for a discussion on the possibility that the central object is a non-black-hole exotic object.

asymptotic behavior of the image of the collapsing object gives us the information about the near horizon geometry which will appear around the collapsing star.

It might be the usual first step to study a simplified model rather than a realistic one. Hence, let us assume the collapsing star to be a spherically symmetric one with uniform density and zero pressure, that is, the Oppenheimer-Snyder collapse [8]. Naively, one may expect that due to the combined effects of the gravitational redshift and the Doppler shift, the frequency of observed photons arriving at the observer from the surface of the star would become smaller and smaller as time goes on, and eventually, it would become undetectable.

This is a classical subject: It was studied in several literatures using the geometric optics approximation, by approximately solving null geodesic equations [9–12] (early works are summarized in p. 847 of [13], and see also [14, 15] for related works). In the early works [9, 10], it was claimed that the dimensionless quantity for the strength of the redshift, $z := \omega'_e/\omega_o - 1$, of the primary photons remains finite as $z \approx 2$ due to approximately circular motion of photons around the photon sphere $r = 3M$, where ω'_e and ω_o are the angular frequencies of emitted photons in the comoving frame attached to the surface of the star and that detected by a distant static observer, respectively. Later, it was pointed out that the above analyses had failed to take into account the contribution of photons that are emitted into the directions almost or just tangential to the surface of the star in its comoving frame, and thus, initially propagate in inward directions in the static frame [11, 12]. Because the Doppler effect causes blueshift for such photons, the value of z of the primary component becomes even smaller. Relatively recently, the same subject was studied but the analyses were restricted to the case that monochromatic waves are emitted from the star surface with a very short period of time [16] or finite duration [17].

Although the subject was tackled more than fifty years ago, as far as we know, this subject has not been fully explored. In the above works, the calculations of spectral radiant flux were limited to the case that the star surface radiates monochromatic waves, and the result is incomplete [10]. Although the formalism for calculating spectral radiant flux has been given in Refs. [16, 17], in the application, approximate solutions are used for null geodesics and primary attention is paid only to the total luminosity and the redshift factor. For this reason, we would like to revisit this problem to derive a formalism for calculating quantities related to photon counting and radiometry, under the condition that the radiator obeys Lambert’s cosine law with arbitrary spectral intensity. In particular, we present expressions

for spectral photon flux and spectral radiant flux that can be directly applied to numerical calculations. We apply our formalism to the two types of radiation: One is monochromatic radiation and the other is blackbody one. This subject is studied with the method of ray tracing, and it turns out that in order to see clearly the behavior of these quantities, highly accurate numerical solutions of many null geodesics propagating from the surface of the star to the static observer are required. If we proceed with it with a personal computer, recent machines are definitely required. Also, we present analytic formulas to describe the late time behavior of observable quantities by developing a method of nonperturbative approximation to photon's worldlines.

One might consider that our analysis does not have a practical application because typically, a collapsing star is surrounded by optically thick plasma, and radiated photons do not directly escape to a distant place. However, our analysis can be applied also to the case of the emission of high-energy neutrinos from, for example, the neutrino-sphere of a collapsing hot neutron star. Even if the plasma surrounding the collapsing star is optically thick for photons, it can be transparent for neutrinos. In order to see time evolution of the spectrum, an observation over a free fall time (e.g., a few hundred μs in the case of the gravitational collapse of a hot neutron star with a few solar masses) is required, and the time resolution of the observation should be much less than the free fall time. The super-Kamiokande has the ability to determine the energy of each neutrino with a time resolution of a few ns [18]. Therefore, our study is a good starting point for predicting the time dependence of the spectrum of high-energy neutrinos emitted from a collapsing star, which will give us information about the near horizon geometry around the collapsing star.

This paper is organized as follows. In the next section, we explain the setup of the problem. In Sec. III, we study null geodesic equations in the Schwarzschild spacetime and present several useful formulas. In Sec. IV, we derive the formulas for observable quantities by photon counting and radiometry. In Sec. V, numerical methods and codes are explained. In Sec. VI, we apply our formalism to two examples, i.e., the cases where the star emits monochromatic radiation and blackbody radiation. In Sec. VII, we develop a nonperturbative approximate method to describe the late time behavior of observable quantities. Analytic formulas for the late time behavior are derived to give support to the numerical results. Section VIII is devoted to a summary and discussions. In the Appendix, an approximate analysis of the redshift factor and some physical quantities near the center of the image are presented.

Throughout the paper, we use basically the units $c = G_N = \hbar = k_B = 1$ where c , G_N , \hbar , and k_B are the speed of light, the Newtonian constant of gravitation, the reduced Planck constant, and the Boltzmann constant, respectively. But they will be recovered if necessary for clarity.

II. SETUP

In this section, the setup of the system is explained. In Sec. II A, we introduce the Oppenheimer-Snyder model of gravitational collapse of a star. In Sec. II B, the properties of radiation from the star surface are specified. The setup on the observer is explained in Sec. II C.

A. Oppenheimer-Snyder collapse

As mentioned in Sec. I, we assume spherical symmetry of the system. The region outside the star is assumed to be vacuum, and hence its geometry is described by the Schwarzschild metric,

$$ds^2 = -f(r)dt^2 + f(r)^{-1}dr^2 + r^2(d\theta^2 + \sin^2\theta d\phi^2), \quad f(r) = 1 - \frac{2M}{r}, \quad (1)$$

where M is a constant that corresponds to the total gravitational mass, i.e., the Arnowitt-Deser-Misner mass in the present case. The star is supposed to be static, to keep its energy density uniform due to the pressure for $t < t_B$, and to begin collapsing at $t = t_B$ due to sudden disappearance of the pressure. The radius of the static star is denoted by R .

By assumption, for $t > t_B$, the star collapses gravitationally. Such a situation is described by the Oppenheimer-Snyder model [8]. The geometry inside the star is given by the Lemître-Friedmann-Robertson-Walker metric,

$$ds^2 = -d\tau^2 + a^2 \left[\frac{d\tilde{R}^2}{1 - k\tilde{R}^2} + \tilde{R}^2(d\theta^2 + \sin^2\theta d\phi^2) \right], \quad (2)$$

with

$$\tau = \frac{1}{2\sqrt{k}}(\xi + \sin\xi), \quad (3a)$$

$$a = \frac{1}{2}(1 + \cos\xi), \quad (3b)$$

for $0 \leq \tilde{R} \leq R$. If we set $k = 2M/R^3$, the two metrics are connected continuously and smoothly at $\tilde{R} = R$.

The world sheet of the star surface coincides with a collection of radial timelike geodesics. Although the result is well known, we explicitly show the geodesic equations and their radial solution for later convenience. The world sheet of the star surface is denoted by $t = t_e(\tau'_e)$ and $r = r_e(\tau'_e)$, where τ'_e is the proper time of the star surface (the subscript “e” indicates that the star surface is an emitter of radiation). Just at the beginning of the gravitational collapse, the star surface is momentarily at rest, i.e., $\dot{r}_e = 0$, and thus the normalization condition of the timelike geodesic tangent leads to $\dot{t}_e = [f(R)]^{-1/2}$, where the dot denotes the derivative with respect to the proper time τ'_e . The t -component of the geodesic equation leads to

$$f(r_e)\dot{t}_e = \sqrt{f(R)}, \quad (4)$$

after integrating once. Then, from the normalization of the timelike geodesic tangent, we have

$$\dot{r}_e = -\sqrt{f(R) - f(r_e)}, \quad (5)$$

where the sign is chosen to be consistent with the fact that the star is collapsing. These two equations can be integrated by using the auxiliary variable ξ in Eqs. (3a) and (3b), and we have

$$\tau'_e = \frac{R}{2} \sqrt{\frac{R}{2M}} (\xi + \sin \xi), \quad (6a)$$

$$r_e = \frac{R}{2} (1 + \cos \xi), \quad (6b)$$

$$t_e - t_B = 2M \log \left[\frac{\sqrt{\frac{R}{2M} - 1} + \tan(\xi/2)}{\sqrt{\frac{R}{2M} - 1} - \tan(\xi/2)} \right] + \sqrt{\frac{R}{2M} - 1} \left[\frac{R}{2} \sin \xi + \left(2M + \frac{R}{2} \right) \xi \right]. \quad (6c)$$

Here, the integral constant is chosen so that $r_e = R$ and $t_e = t_B$ at $\tau'_e = 0$. The surface of the star crosses the horizon at

$$\xi = \xi_h := 2 \arctan \sqrt{\frac{R}{2M} - 1} \quad (7)$$

and t_e diverges there reflecting the fact that the Schwarzschild time t becomes degenerate on the horizon.

B. Radiation from the star surface

In this paper, we assume that radiation is emitted from the star surface in accordance with Lambert's cosine law. If dN number of photons are emitted from a surface in the interval $d\tau'_e$ of its proper time, photon flux is defined as

$$\mathcal{F}_e^{(N)} = \frac{dN}{d\tau'_e}, \quad (8)$$

where the superscript “(N)” of $\mathcal{F}_e^{(N)}$ is added to stress that we are considering the photon number flux (not the radiation energy flux). The photon flux within an infinitesimal interval of angular frequency $d\omega_e$ emitted from an areal element dS'_e on the star surface within an infinitesimal solid angle $d\Omega'_e$ with the direction at an angle ϑ'_e to the normal of the area element is given by

$$d^3\mathcal{F}_e^{(N)} = I_e^{(N)} \cos \vartheta'_e d\Omega'_e dS'_e d\omega'_e, \quad (9)$$

Here, $I_e^{(N)}$ is called spectral photon radiance.² In general, $I_e^{(N)}$ is a function of time τ'_e , angular frequency ω'_e , and the angle ϑ'_e . If $I_e^{(N)}$ does not depend on the angle ϑ'_e , the radiation is said to follow Lambert's cosine law. Here, all quantities with prime are measured in the comoving frame of the star surface, or more precisely, with respect to the tetrad frame,

$$(e'_0)_\mu = (-f(r_e)\dot{t}_e, f^{-1}(r_e)\dot{r}_e, 0, 0), \quad (10a)$$

$$(e'_1)_\mu = (-\dot{r}_e, \dot{t}_e, 0, 0), \quad (10b)$$

$$(e'_2)_\mu = (0, 0, r_e, 0), \quad (10c)$$

$$(e'_3)_\mu = (0, 0, 0, r_e \sin \theta). \quad (10d)$$

Note that by virtue of Eqs. (4) and (5), each component of $(e'_0)_\mu$ and $(e'_1)_\mu$ becomes a function of r_e . Introducing the null vector tangent to the worldline of an emitted photon from the star surface as

$$k^\mu := \frac{dx^\mu}{d\lambda} = (t_{,\lambda}, r_{,\lambda}, 0, \phi_{,\lambda}), \quad (11)$$

where the worldline is a geodesic parametrized by the affine parameter λ , the angle ϑ'_e is given by

$$\tan \vartheta'_e = \frac{k^\mu (e'_3)_\mu}{k^\nu (e'_1)_\nu}, \quad (12)$$

² In terms of radiated energy E_e , the spectral radiance $I_e^{(E)}$ is introduced by $d^3(dE_e/d\tau'_e) = I_e^{(E)} \cos \vartheta'_e d\Omega'_e dS'_e d\omega'_e$. The two kinds of radiance are related as $I_e^{(E)} = \omega'_e I_e^{(N)}$ in the unit $\hbar = 1$.

in terms of the tetrad vectors, Eqs. (10a)–(10d). Note that due to the spherical symmetry, it is sufficient to consider geodesics in the equatorial plane $\theta = \pi/2$.

The value of $I_e^{(N)}$ may change as the collapse proceeds. Since the radius of the star surface r_e is a monotonically decreasing function of time, $I_e^{(N)}$ is regarded as a function of not only ω'_e but also r_e , i.e., $I_e^{(N)}(r_e, \omega'_e)$. We also introduce the following quantity called photon radiance,

$$J_e^{(N)}(r_e) := \int_0^\infty I_e^{(N)}(r_e, \omega'_e) d\omega'_e. \quad (13)$$

The photon radiance and the photon flux are related as

$$d^2 \mathcal{F}_e^{(N)} = J_e^{(N)}(r_e) \cos \vartheta'_e d\Omega'_e dS'_e. \quad (14)$$

In this paper, we develop a formalism to calculate observable quantities, in particular, spectral photon flux and spectral radiant flux for arbitrary $I_e^{(N)}(r_e, \omega'_e)$. We apply our formalism to radiation with the following two kinds of spectra.

1. Monochromatic radiation

The first case is that the emitted radiation is monochromatic with the angular frequency $\bar{\omega}'_e$. In this case, $I_e^{(N)}$ takes the form

$$I_e^{(N)}(r_e, \omega'_e) = J_e^{(N)}(r_e) \delta(\omega'_e - \bar{\omega}'_e). \quad (15)$$

In addition, we assume that $J_e^{(N)}(r_e)$ be constant throughout the collapse for simplicity:

$$J_e^{(N)}(r_e) \equiv J. \quad (16)$$

The extension to the case that $J(r_e)$ varies in time is straightforward.

2. Blackbody radiation

The second case is blackbody radiation. In this case, we have

$$I_e^{(N)}(\omega'_e, r_e) = \frac{\omega_e'^2}{4\pi^3 [\exp(\omega'_e/T'_e) - 1]}. \quad (17)$$

Note that we are adopting the unit $\hbar = k_B = 1$, and this formula is not for the energy flux but for the photon flux. For this formula, $J_e^{(N)}(r_e)$ is calculated as

$$J_e^{(N)}(r_e) = \frac{\zeta(3)}{2\pi^3} T_e'^3. \quad (18)$$

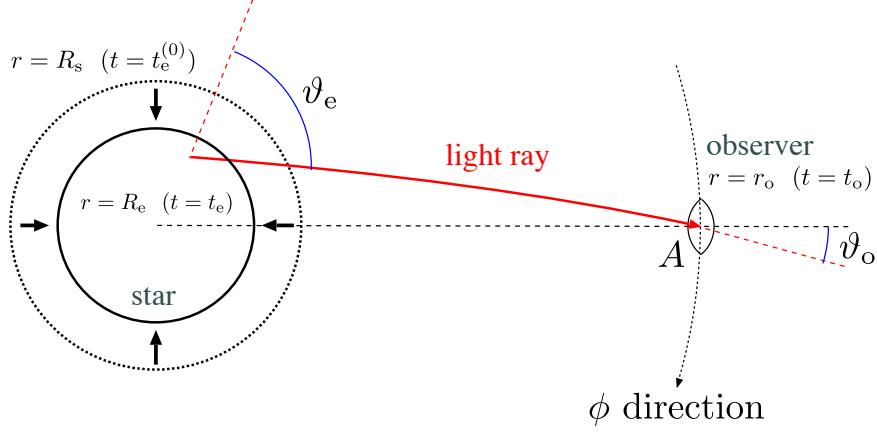


FIG. 1: Setup of the system and an example of a light ray.

In general, $I_e^{(N)}(\omega'_e, r_e)$ and $J_e^{(N)}(r_e)$ are dependent on r_e through the change in the temperature T'_e . In this paper, for simplicity, we assume

$$T'_e = \text{constant}, \quad (19)$$

and therefore, the value of $I_e^{(N)}(\omega'_e)$ does not depend on the radius of the star surface.

C. The observer

Figure 1 is a schematic picture of relative positions of the collapsing star and the observer. The observer is at rest with respect to the Schwarzschild frame at the radius r_o . More specifically, the observer's worldline in the four-dimensional spacetime is parametrically given by $t = t_o(\tau_o)$, $r = r_o(\tau_o)$, $\theta = \theta_o(\tau_o)$, and $\phi = \phi_o(\tau_o)$, where τ_o is the proper time of the observer (the subscript "o" indicates the observer). By assumption, r_o , θ_o and ϕ_o are constant. Because the spacetime is spherically symmetric, we set $\theta_o = \pi/2$, $\phi_o = 0$ without loss of generality. The proper time τ_o and the coordinate time t_o are related as $d\tau_o/dt_o = \sqrt{f(r_o)}$. Furthermore, we assume that r_o is much larger than the radius of the initial star surface R . The observer detects photons from the star surface using a telescope, and determines the photon/radiant flux with respect to the proper time τ_o of the observer. The telescope is directed toward the center of the star, and its lens has the area A . In the following sections, we calculate the flux of photon number and the flux of photon energy that come into the telescope through its lens.

We determine the origin of time coordinate t so that the observer finds that the star begins to collapse at $t_o = 0$. A radially propagating photon emitted from $r = R$ takes a period of time \mathcal{T} given by

$$\mathcal{T} = r_o - R + 2M \log \left(\frac{r_o - 2M}{R - 2M} \right), \quad (20)$$

in order to arrive at the observer staying at $r = r_o$. Hence, the beginning time of the gravitational collapse, t_B , introduced in the paragraph including Eq. (1) is equal to $-\mathcal{T}$. Note that the observer finds that the star begins to collapse through the time variation in the redshift at the center of the image.

III. NULL GEODESICS IN THE SCHWARZSCHILD SPACETIME

In the geometric optics approximation, all the information we need about detected photons (e.g., the angular frequency and the photon flux) are included in the null geodesic congruence that connects the emitter with the observer. In this section, we explain basic properties of null geodesics in this spacetime. Useful analytic formulas are also presented.

An example of a light ray is depicted in Fig. 1. A photon is emitted from the star surface at $(t, r) = (t_e, r_e)$ and arrives at the observer at $(t, r) = (t_o, r_o)$. At the emission and observation events, we introduce the angles ϑ_e and ϑ_o , respectively, between the spatial direction of photon's motion and the outward radial direction measured in the static frame. To be more precise, introducing the tetrad basis associated with the static frame,

$$(e_0)_\mu = (-f^{1/2}, 0, 0, 0), \quad (21a)$$

$$(e_1)_\mu = (0, f^{-1/2}, 0, 0), \quad (21b)$$

$$(e_2)_\mu = (0, 0, r, 0), \quad (21c)$$

$$(e_3)_\mu = (0, 0, 0, r \sin \theta), \quad (21d)$$

and the tangent vector of the null geodesic given by Eq. (11), ϑ_e and ϑ_o are defined as

$$\tan \vartheta_e = \frac{k^\mu (e_3)_\mu}{k^\nu (e_1)_\nu} \bigg|_{(t,r)=(t_e,r_e)}, \quad \tan \vartheta_o = \frac{k^\mu (e_3)_\mu}{k^\nu (e_1)_\nu} \bigg|_{(t,r)=(t_o,r_o)}. \quad (22)$$

Here, note that ϑ_e is different from ϑ'_e introduced in Eq. (9), and these two quantities must be distinguished.

Here, we mention the basic idea of the ray tracing method whose numerical details will be presented in Sec. V. Let us consider a photon that comes into the telescope at $t = t_o$ with the angle ϑ_o . By numerically solving the null geodesic equation

$$\frac{dk^\mu}{d\lambda} + \Gamma^\mu_{\alpha\beta} k^\alpha k^\beta = 0, \quad (23)$$

backward in time, we obtain the worldline of the photon in the form, $t = t(\lambda)$, $r = r(\lambda)$, $\theta = \pi/2$ and $\phi = \phi(\lambda)$. If the value of ϑ_o is not too large, the worldline of the photon intersects the world sheet of the star surface, which is given by Eqs. (6b) and (6c). The intersection corresponds to the event of photon emission from the star surface.

For a photon traveling in the equatorial plane $\theta = \pi/2$, the geodesic equations (23) lead to the conservation laws for energy and angular momentum of a photon,

$$ft_{,\lambda} = E_{\text{ph}}, \quad (24a)$$

$$r^2\phi_{,\lambda} = bE_{\text{ph}}, \quad (24b)$$

by integrating t and ϕ components once, respectively, where E_{ph} and b are integral constants corresponding to the energy and the impact parameter of the photon, respectively. The null condition $k_\mu k^\mu = 0$ becomes

$$ft_{,\lambda}^2 = f^{-1}r_{,\lambda}^2 + r^2\phi_{,\lambda}^2. \quad (24c)$$

From Eqs. (24a)–(24c), we have

$$\frac{dr}{dt} = \pm f \sqrt{1 - \frac{b^2 f}{r^2}}, \quad (25a)$$

$$\frac{d\phi}{dt} = \frac{bf}{r^2}. \quad (25b)$$

Here, we would like to make a remark on a previous work. When the sign of Eq. (25a) is plus (respectively, minus), the photon is moving outward (respectively, inward). As we will see in Fig. 4 later, there are photons that initially travel inward but turn outward and arrive at the observer. In this case, the right-hand side of Eq. (25a) changes its sign during the propagation. Since it is difficult to handle such an equation numerically, we solve the second-order differential equation for r instead of Eq. (25a) (see Sec. V). By contrast, the analysis of Ref. [10] used Eq. (25a) only with the plus sign, and thus, it has missed the contribution from photons that change the sign of Eq. (25a).

Below, we list up the useful relations that will be used later. These relations can be used also to check the accuracy of numerical calculations.

A. Radial photon orbit

In the case of $b = 0$, photons propagate in the radial direction. Equations (25a) and (25b) are integrated as $\phi = \text{const}$, and

$$t - t_o = r - r_o + 2M \log \left(\frac{r - 2M}{r_o - 2M} \right), \quad (26)$$

where we have chosen the plus sign of Eq. (25a). Equation (20) is based on this formula: The value of \mathcal{T} is obtained by substituting $(t, r) = (-\mathcal{T}, R)$ and $t_o = 0$ into Eq. (26).

B. Photon orbit with critical impact parameter

Another special case where worldlines of photons are analytically obtained is that the impact parameter b has the following value:

$$b_{\text{crit}} := 3\sqrt{3}M, \quad (27)$$

where b_{crit} is called the critical impact parameter. Setting $b = b_{\text{crit}}$, Eq. (25a) becomes

$$\frac{dt}{dr} = \pm \frac{r^{5/2}}{(r - 2M)(r - 3M)\sqrt{r + 6M}}. \quad (28)$$

It is seen that $r = 3M$ for arbitrary t is a solution to this equation, which represents the worldline of a circularly orbiting photon. Below, we solve for worldlines of photons whose radial positions change in time. This equation can be integrated as

$$t = \pm F(r) + \text{const}, \quad (29)$$

where the function $F(r)$ is given by

$$F(r) = \bar{F}(r) - 3\sqrt{3}M \log \left| \frac{\sqrt{3r} + \sqrt{r + 6M}}{\sqrt{3r} - \sqrt{r + 6M}} \right| \quad (30)$$

with

$$\bar{F}(r) := \sqrt{r(r + 6M)} + 4M \log \left(\sqrt{\frac{r}{M}} + \sqrt{\frac{r}{M} + 6} \right) + 2M \log \left(\frac{2\sqrt{r} + \sqrt{r + 6M}}{2\sqrt{r} - \sqrt{r + 6M}} \right). \quad (31)$$

Because $F(r)$ diverges at $r = 3M$, these worldlines never cross $r = 3M$. For this reason, $t = F(r)$ implicitly includes two kinds of solutions: $t = F^{(\text{out})}(r)$ with

$$F^{(\text{out})}(r) := F(r)|_{3M < r < \infty}, \quad (32)$$

whose worldline is confined in the outside region $3M < r < \infty$, and $t = F^{(\text{in})}(r)$ with

$$F^{(\text{in})}(r) = F(r)|_{2M < r < 3M}. \quad (33)$$

whose worldline is confined in the inside region $2M < r < 3M$. As a result, we have four kinds of solutions, $t = \pm F^{(\text{out})}(r) + \text{const}$ and $t = \pm F^{(\text{in})}(r) + \text{const}$, in total.

Among these four solutions, the solution of special importance is

$$t - t_o = F^{(\text{out})}(r) - F^{(\text{out})}(r_o). \quad (34)$$

This solution represents a worldline of a photon that originally orbits in the domain very close to a circle on $r = 3M$ in the past, but gradually leaves that domain outward and arrives at the observation point $(t, r) = (t_o, r_o)$. For $t \ll -M$, this orbit is approximated as

$$\frac{r}{M} - 3 \approx \exp \left[\frac{t - t_o - C + F(r_o)}{3\sqrt{3}M} \right] \quad (35)$$

with

$$\frac{C}{M} = 3\sqrt{3} + 4 \log(\sqrt{3} + 3) + 2 \log \left(\frac{2\sqrt{3} + 3}{2\sqrt{3} - 3} \right) - 3\sqrt{3} \log 18. \quad (36)$$

As will be shown in Secs. VI and VII, this orbit plays a crucial role for the late time behavior of observables.

In Sec. VII, two other kinds of solutions, $t = -F^{(\text{out})}(r)$ and $t = -F^{(\text{in})}(r)$, will be used. These solutions represent worldlines of photons that asymptotically approach the photon sphere for large t from the outside and inside regions, respectively.

C. Relation between r_e (r_o) and ϑ_e (ϑ_o)

Due to the conservation laws (24a) and (24b) of a photon and the null condition (24c), the tangent vectors k^μ of a geodesic of a photon, Eq. (11), is written in terms of E_{ph} , b , and r . At the points of the emission and observation events, the tangent vectors can be rewritten as

$$k^\mu|_{r=r_e} = E_{\text{ph}}(f(r_e)^{-1}, \cos \vartheta_e, 0, r_e^{-1} f(r_e)^{-1/2} \sin \vartheta_e), \quad (37a)$$

$$k^\mu|_{r=r_o} = E_{\text{ph}}(f(r_o)^{-1}, \cos \vartheta_o, 0, r_o^{-1} f(r_o)^{-1/2} \sin \vartheta_o), \quad (37b)$$

by eliminating b using the definitions for ϑ_e and ϑ_o in Eq. (22), respectively. Then, the conservation of the angular momentum, Eq. (24b), implies

$$b = \frac{r_e}{\sqrt{f(r_e)}} \sin \vartheta_e = \frac{r_o}{\sqrt{f(r_o)}} \sin \vartheta_o. \quad (38)$$

From this relation, we can read off the following two implications. First, for a given r_o , Eq. (38) implies that there is correspondence between b and ϑ_o , which is one-to-one for $|\vartheta_o| \leq \pi/2$. Therefore, one can specify the angle ϑ_o of arriving photons using the value of b instead. Second, for a given b , the value of $\sin \vartheta_e$ can be determined once the value of r_e is specified. These facts will be used in our numerical calculation.

D. Relation between ϑ_e and ϑ'_e

ϑ_e and ϑ'_e have been defined as the angles between the spatial direction of photon's motion and the outward radial direction measured in the static and comoving frames, respectively. In order to find the relation between these two angles, let us introduce (the absolute value of) the velocity β of the star surface measured in the static frame. Since $(e'_0)^\mu$ is equivalent to the four-velocity of the star surface, we have

$$\beta := \left| \frac{(e'_0)^\mu (e_1)_\mu}{(e'_0)^\nu (e_0)_\nu} \right| = -f^{-1}(r_e) \frac{\dot{r}_e}{\dot{t}_e} = \sqrt{1 - \frac{f(r_e)}{f(R)}}. \quad (39)$$

It can be checked that the comoving frame is related to the static frame through the boost transformation,

$$(e'_0)^\mu = \gamma [(e_0)^\mu - \beta (e_1)^\mu], \quad (40a)$$

$$(e'_1)^\mu = \gamma [-\beta (e_0)^\mu + (e_1)^\mu], \quad (40b)$$

$$(e'_2)^\mu = (e_2)^\mu, \quad (40c)$$

$$(e'_3)^\mu = (e_3)^\mu, \quad (40d)$$

where $\gamma = 1/\sqrt{1 - \beta^2}$. From Eqs. (12) and (22), we have

$$\cos \vartheta_e = \frac{\cos \vartheta'_e - \beta}{1 - \beta \cos \vartheta'_e}. \quad (41)$$

One of the implications of this relation is as follows. Let us consider photons making the limb of the observed image. Such photons are emitted in the directions tangential to the star surface in the comoving frame, i.e., $\vartheta'_e = \pi/2$. Equation (41) leads to

$$\cos \vartheta_e = -\sqrt{1 - \frac{f(r_e)}{f(R)}} \quad (42)$$

for these photons, and thus the value of ϑ_e is greater than $\pi/2$. This fact implies that these photons are emitted in the inward direction in the static frame.

IV. OBSERVABLE QUANTITIES

In this section, we present a formalism to calculate observable quantities. The derivations of the redshift, the quantities related to photon counting, and the quantities related to radiometry are shown here, one by one.

A. Redshift

In describing the strength of the redshift of photons, the quantity $z := \omega'_e/\omega_o - 1$ is commonly used, where ω_o and ω'_e are angular frequency of observed photons and of emitted photons, respectively. But in this paper, instead of z , we use

$$\alpha := \frac{1}{1+z} = \frac{\omega_o}{\omega'_e}. \quad (43)$$

We call α the redshift factor. The angular frequency of a photon at the emission event is

$$\omega'_e := -k^\mu (e'_0)_\mu|_{r=r_e} \quad (44)$$

where, as mentioned, $(e'_0)^\mu$ is equivalent to the four-velocity of the star surface. The angular frequency of an observed photon is

$$\omega_o := -k^\mu (e_0)_\mu|_{r=r_o} \quad (45)$$

where $(e_0)^\mu$ has been introduced in Eq. (21a) which is equivalent to the four-velocity of the observer. For a fixed observation point (t_o, r_o) , all arriving photons with a fixed angle ϑ_o have the same value of the redshift factor α . Since there is a one-to-one relation between b and ϑ_o by virtue of Eq. (38), α is regarded a function of the impact parameter b and observer's coordinate time t_o .

In order to derive an expression for α , it is convenient to consider the gravitational redshift from the star surface to the observer,

$$\frac{k^\mu (e_0)_\mu|_{r=r_o}}{k^\nu (e_0)_\nu|_{r=r_e}} = \sqrt{\frac{f(r_e)}{f(r_o)}}, \quad (46)$$

which is derived from Eqs. (21a), (37a), and (37b), and the Doppler effect coming from the relative motion of the star surface to the static frame,

$$\frac{k^\mu (e_0)_\mu|_{r=r_o}}{k^\nu (e'_0)_\nu|_{r=r_e}} = \frac{\gamma^{-1}}{1 + \beta \cos \vartheta_e}, \quad (47)$$

which is derived from Eqs. (21a), (21b), (37a), and (40a). Multiplication of Eqs. (46) and (47) corresponds to the redshift factor Eq. (43), and hence, we have

$$\alpha = \frac{f(r_e)}{\sqrt{f(R)f(r_o)}} \left(1 + \cos \vartheta_e \sqrt{1 - \frac{f(r_e)}{f(R)}} \right)^{-1}. \quad (48)$$

For a given impact parameter b , the value of $\sin \vartheta_e$ is given in terms of r_e from Eq. (38). Then, $\cos \vartheta_e$ has two possible values, $\cos \vartheta_e = \pm \sqrt{1 - \sin^2 \vartheta_e}$, and plus (respectively, minus) sign corresponds to an outwardly (respectively, inwardly) emitted photon. Therefore, the value of α can be determined if we specify the radius r_e of the star surface and the direction of propagation of a photon at the emission event.

By using Eqs. (39) and (41), Eq. (48) is rewritten in the form

$$\alpha = \sqrt{\frac{f(R)}{f(r_o)}} \left(1 - \cos \vartheta'_e \sqrt{1 - \frac{f(r_e)}{f(R)}} \right). \quad (49)$$

In the case of $\vartheta'_e = \pi/2$, as mentioned, photons are emitted in the tangential direction to the star surface in the comoving frame and make the limb of the observed image. The redshift factor of such photons is equal to

$$\alpha_{\text{limb}} := \alpha|_{\vartheta'_e=\pi/2} = \sqrt{\frac{f(R)}{f(r_o)}}. \quad (50)$$

Therefore, the redshift factor on the limb of the image is unchanged throughout the collapse. This happens because such photons initially propagate in the inward direction in the static frame, and thus, the Doppler effect causes the blueshift, which cancels out the increase in the gravitational redshift.

As discussed in Secs. III A and III B, worldlines of null geodesics for $b = 0$ and $b = b_{\text{crit}}$ are given in the analytic forms, Eq. (26) and Eq. (34) with Eqs. (30)–(32), respectively. Therefore, the redshift factor can be calculated analytically for photons with these values of b as functions of observer's time t_o . The result is shown in Fig. 2. Hereafter, the values of the redshift factor α for $b = 0$ and $b = b_{\text{crit}}$ are denoted by

$$\alpha_{\text{cent}} := \alpha|_{b=0}, \quad (51)$$

$$\alpha_{\text{crit}} := \alpha|_{b=b_{\text{crit}}}, \quad (52)$$

respectively, where the subscript “cent” indicates the center of the star image, $\vartheta_o = 0$. The value of α_{cent} decays to zero, and its late time behavior is approximately proportional to

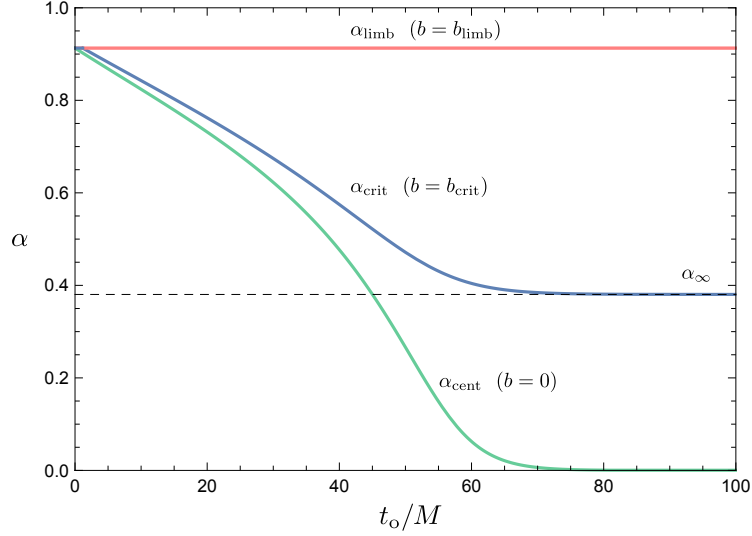


FIG. 2: The values of the redshift factor α_{cent} , α_{crit} , and α_{limb} for $b = 0$, b_{crit} and b_{limb} , respectively, as functions of observer's time t_o . The value of α_{crit} asymptotes to α_{∞} given by Eq. (53).

$\exp(-t_o/4M)$ (see the Appendix). The redshift factor α_{crit} for $b = b_{\text{crit}}$ asymptotes to a constant value α_{∞} . The value of α_{∞} is obtained by setting $r_e = 3M$ and $\vartheta_e = \pi/2$ in Eq. (48), because in the limit of $t_o \rightarrow \infty$, the analytic expression, Eq. (34) with Eqs. (30)–(32), for the worldline of a photon with $b = b_{\text{crit}}$ suggests that the photon is emitted from the star surface precisely on the photon sphere $r = 3M$ in the tangential direction to it. This leads to

$$\alpha_{\infty} = \frac{f(3M)}{\sqrt{f(R)f(r_o)}}. \quad (53)$$

By virtue of Eq. (35), the value of α_{crit} asymptotes to α_{∞} in the manner that the value of $\alpha_{\text{crit}} - \alpha_{\infty}$ is approximately proportional to $\exp(-t_o/3\sqrt{3}M)$. The value of α_{limb} , i.e., the redshift factor of photons on the limb whose impact parameter is denoted by b_{limb} , is also shown in Fig. 2. Note that although α_{limb} is a constant throughout the collapse, b_{limb} itself is time dependent, and its behavior must be determined numerically. In order to obtain the redshift factors of photons with other impact parameters, we have to perform numerical calculations.

B. Photon counting

In photon counting, individual photons are counted using some single-photon detector. If dN photons are counted in a time interval $d\tau_o$, photon flux is determined by

$$\mathcal{F}^{(N)} := \frac{dN}{d\tau_o}. \quad (54)$$

Below, we derive the formulas to calculate the photon intensity, the photon flux, and spectral photon intensity. Before starting, we briefly discuss the angular range of ϑ_o of the image of the star and the range of the impact parameter b of arriving photons for a later convenience.

The image of the star has the shape of a disk. The center and the limb of the image are composed of photons with $b = 0$ and $b = b_{\text{limb}}$, respectively, whereas the other part of the image is composed of photons with $0 < b < b_{\text{limb}}$. The angular diameter of the image is equal to $2\vartheta_o^{(\text{limb})}$, where $\vartheta_o^{(\text{limb})}$ is related to b_{limb} through Eq. (38) as

$$b_{\text{limb}} = \frac{r_o}{\sqrt{f(r_o)}} \sin \vartheta_o^{(\text{limb})}. \quad (55)$$

Since b_{limb} depends on the observer's time as mentioned before, we denote it as $b_{\text{limb}}(t_o)$. The initial value of b_{limb} , i.e. $b_{\text{limb}}(0)$, is obtained by setting $\vartheta_e = \pi/2$ and $r_e = R$ in Eq. (38) as

$$b_{\text{limb}}(0) = \frac{R}{\sqrt{f(R)}}. \quad (56)$$

See Sec. VIA for more information about the behavior of $b_{\text{limb}}(t_o)$.

1. Photon intensity

Photon intensity is a quantity that is useful in observing an object whose image has a finite size. It is defined as photon flux per unit solid angle observed by a telescope, $d\mathcal{F}^{(N)}/d\Omega_o$. Photon intensity is a directional quantity.

Let us derive the formula to calculate this quantity. As shown in the left picture of Fig. 3, we consider a ray bundle that has a vertex with the infinitesimal solid angle $d\Omega_o$ at the observation point. Evolving the ray bundle backward in time, it intersects the star surface at the area element dS'_e at the angle ϑ'_e to the normal to the area element (in the comoving frame). These two quantities are related to each other through the angular diameter distance D as

$$dS'_e \cos \vartheta'_e = D^2 d\Omega_o. \quad (57)$$

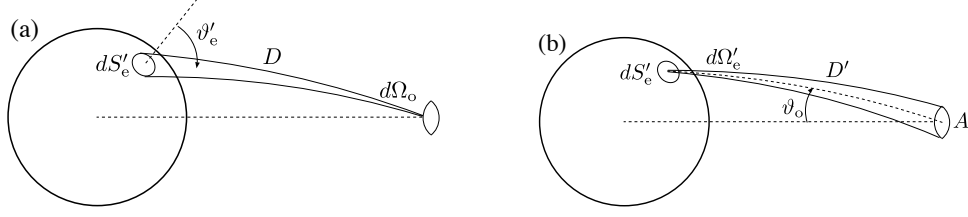


FIG. 3: Definitions of (a) the angular diameter distance D and (b) the corrected luminosity distance D' . See text for details.

Alternatively, we can consider a ray bundle with a vertex at the center of the area element dS'_e on the star surface. We suppose that at the vertex, the ray bundle have an infinitesimal solid angle $d\Omega'_e$ such that it exactly intersects the lens of the telescope with the area A after evolving forward in time (the right-hand side of Fig. 3). The relation between these two quantities is expressed as

$$A \cos \vartheta_o = D'^2 d\Omega'_e. \quad (58)$$

Here, the quantity D' is called the corrected luminosity distance [19]. These two relations (57) and (58) with Eqs. (8) and (14) give

$$d \left(\frac{dN}{d\tau'_e} \right) = J_e^{(N)}(r_e) A \left(\frac{D}{D'} \right)^2 \cos \vartheta_o d\Omega_o. \quad (59)$$

Here, we use the *reciprocity relation*,

$$D/D' = \omega_o/\omega'_e =: \alpha, \quad (60)$$

which is a well-known relation in the context of gravitational lensing [20] (see also [19]). Note that this relation can be applied to the cases that both the star and the observer are moving relatively: The effects of the relativistic beaming and the time delay caused by relativistic motion and strong gravity are all included in this formula. The two time intervals $d\tau'_e$ and $d\tau_o$, during which the same dN photons are emitted and observed, are related as $\omega'_e d\tau'_e = \omega_o d\tau_o$. Then, we have the formula for the photon intensity,

$$\frac{d\mathcal{F}^{(N)}}{d\Omega_o} = J_e^{(N)}(r_e) A \alpha^3 \cos \vartheta_o. \quad (61)$$

We normalize this quantity by the initial value of the photon flux, $\mathcal{F}^{(N)}(0)$. The initial photon flux can be calculated by setting $r_e = R$ and $\alpha = \alpha_{\text{limb}}$ with Eq. (50), and by

integrating Eq. (61) with respect to the solid angle in the range $0 \leq \vartheta_o \leq \vartheta_o^{(\text{limb})}(0)$. The result is

$$\mathcal{F}^{(N)}(0) = \pi J_e^{(N)}(R) A \sqrt{\frac{f(R)}{f(r_o)}} \left(\frac{R}{r_o}\right)^2. \quad (62)$$

Therefore, we have

$$\frac{[d\mathcal{F}^{(N)}/d\Omega_o](t_o)}{\mathcal{F}^{(N)}(0)} = \pi^{-1} \left(\frac{r_o}{R}\right)^2 \sqrt{\frac{f(r_o)}{f(R)}} \frac{J_e^{(N)}(r_e)}{J_e^{(N)}(R)} \alpha^3 \cos \vartheta_o. \quad (63)$$

Here, r_e is the radius of the star at the moment when photons arriving at the telescope at the observer's coordinate time t_o with the angle ϑ_o were emitted. Namely, similarly to the redshift factor α , the quantity r_e is regarded as a function of (ϑ_o, t_o) .

2. Photon flux

The photon flux can be obtained by integrating Eq. (63) with respect to the solid angle $d\Omega_o = 2\pi \sin \vartheta_o d\vartheta_o$. By using the integration by substitution with the relation between b and ϑ_o in Eq. (38), we have

$$\frac{\mathcal{F}^{(N)}(t_o)}{\mathcal{F}^{(N)}(0)} = \frac{2}{R^2} \sqrt{\frac{f(r_o)^3}{f(R)}} \int_0^{b_{\text{limb}}} \frac{J_e^{(N)}(r_e)}{J_e^{(N)}(R)} \alpha^3 b \, db. \quad (64)$$

3. Spectral photon flux

Spectral photon flux is defined as the photon flux per unit angular frequency interval, $d\mathcal{F}^{(N)}/d\omega_o$. In order to derive the formula for this quantity, first we derive the spectral photon flux within an infinitesimal solid angle $d\Omega_o$ and then, integrate it with respect to the solid angle.

The derivation is similar to that of the photon intensity. Using the relations (57) and (58) with Eqs. (8) and (9), we have

$$d^2 \left(\frac{dN}{d\tau'_e} \right) = I_e^{(N)}(r_e, \omega'_e) A \left(\frac{D}{D'} \right)^2 \cos \vartheta_o d\Omega_o d\omega'_e. \quad (65)$$

Because photons emitted with an angular frequency ω'_e arrive at the observation point as photons with angular frequency $\omega_o = \alpha\omega'_e$, we have³

$$d^2 \mathcal{F}^{(N)} = I_e^{(N)}(r_e, \omega_o/\alpha) A \alpha^2 \cos \vartheta_o d\Omega_o d\omega_o. \quad (66)$$

³ Defining spectral photon radiance received by the telescope as $I_o^{(N)} := d^2 \mathcal{F}^{(N)}/A \cos \vartheta_o d\Omega_o d\omega_o$, we have

Here, we used the reciprocity relation (60) and the relation between the two time intervals, $\omega'_e d\tau'_e = \omega_o d\tau_o$. If we integrate this formula with respect to ω_o , the formula for the photon intensity (61) is recovered. Integrating with respect to the solid angle and normalizing with $\mathcal{F}^{(N)}(0)$, we have

$$\frac{[d\mathcal{F}^{(N)}/d\omega_o](t_o)}{\mathcal{F}^{(N)}(0)} = \frac{2}{R^2} \sqrt{\frac{f(r_o)^3}{f(R)}} \int_0^{b_{\text{limb}}} \frac{I_e^{(N)}(r_e, \omega_o/\alpha)}{J_e^{(N)}(R)} \alpha^2 b \, db. \quad (67)$$

C. Radiometry

Now, we derive formulas for quantities related to radiometry. In radiometry, the energy of received electromagnetic radiation is measured. If radiant energy dE_o passes through the lens and is received by the telescope in the interval $d\tau_o$ of its proper time, the radiant flux, or equivalently, the energy flux of photons is defined by

$$\mathcal{F}^{(E)} := \frac{dE_o}{d\tau_o}. \quad (68)$$

Similarly to the case of photon counting, radiant intensity is defined as the radiant flux per unit solid angle, $d\mathcal{F}^{(E)}/d\Omega_o$, and spectral radiant flux is defined as the radiant flux per unit angular frequency interval, $d\mathcal{F}^{(E)}/d\omega_o$.

Since one photon has the energy $\hbar\omega_o$ at the observation event, the radiant flux for an infinitesimal solid angle $d\Omega_o$ and an infinitesimal angular frequency interval $d\omega_o$ is given by

$$d^2\mathcal{F}^{(E)} = \omega_o d^2\mathcal{F}^{(N)} \quad (69)$$

(in the unit $\hbar = 1$), where $d^2\mathcal{F}^{(N)}$ is given in Eq. (66). Once Eq. (69) is given, we obtain the radiant intensity $d\mathcal{F}^{(E)}/d\Omega_o$ and the spectral radiant flux $d\mathcal{F}^{(E)}/d\omega_o$ by integrating Eq. (69) with the angular frequency and the solid angle, respectively.

We choose the initial radiant flux $\mathcal{F}^{(E)}(0)$ as the normalization factor. Integrating $d^2\mathcal{F}^{(E)}$ with both the solid angle and the angular frequency for the initial value $r_e = R$ and $\alpha = \alpha_{\text{limb}}$ with Eq. (50), we have

$$\mathcal{F}^{(E)}(0) = \langle \omega'_e \rangle|_R \sqrt{\frac{f(R)}{f(r_o)}} \mathcal{F}^{(N)}(0). \quad (70)$$

the relation $I_o^{(N)}/\omega_o^2 = I_e^{(N)}/\omega'_e{}^2$ from Eq. (66). In terms of spectral radiance, $I_o^{(E)} := \omega_o I_o^{(N)}$ and $I_e^{(E)} := \omega'_e I_e^{(N)}$, we recover the conserved relation $I_o^{(E)}/\omega_o^3 = I_e^{(E)}/\omega'_e{}^3$ [9, 10].

Here, we have introduced the mean value of the angular frequency of emitted photons in the comoving frame,

$$\langle \omega'_e \rangle|_{r_e} := \frac{\int_0^\infty \omega'_e I_e^{(N)}(r_e, \omega'_e) d\omega'_e}{J_e^{(N)}(r_e)}. \quad (71)$$

Then, we have

$$\frac{d^2 \mathcal{F}^{(E)}}{\mathcal{F}^{(E)}(0)} = \pi^{-1} \left(\frac{r_o}{R} \right)^2 \frac{f(r_o)}{f(R)} \alpha^2 \cos \vartheta_o d\Omega_o \frac{I_e^{(N)}(r_e, \alpha^{-1} \omega_o)}{J_e^{(N)}(R)} \frac{\omega_o}{\langle \omega'_e \rangle|_R} d\omega_o. \quad (72)$$

1. Radiant intensity

Integrating Eq. (72) with respect to the angular frequency ω_o , we obtain the formula for the radiant intensity,

$$\frac{[d\mathcal{F}^{(E)}/d\Omega_o](t_o)}{\mathcal{F}^{(E)}(0)} = \pi^{-1} \left(\frac{r_o}{R} \right)^2 \frac{f(r_o)}{f(R)} \frac{J_e^{(N)}(r_e)}{J_e^{(N)}(R)} \frac{\langle \omega'_e \rangle|_{r_e}}{\langle \omega'_e \rangle|_R} \alpha^4 \cos \vartheta_o. \quad (73)$$

The radiant intensity is also called the surface brightness in astronomy.

2. Radiant flux

Integrating Eq. (73) with respect to the solid angle and rewriting ϑ_o in the integral with b using Eq. (38), we obtain the formula for the radiant flux,

$$\frac{\mathcal{F}^{(E)}(t_o)}{\mathcal{F}^{(E)}(0)} = \frac{2}{R^2} \frac{f(r_o)^2}{f(R)} \int_0^{b_{\text{limb}}} \frac{J_e^{(N)}(r_e)}{J_e^{(N)}(R)} \frac{\langle \omega'_e \rangle|_{r_e}}{\langle \omega'_e \rangle|_R} \alpha^4 b \, db. \quad (74)$$

3. Spectral radiant flux

Integrating Eq. (72) with respect to the solid angle and rewriting ϑ_o in the integral with b using Eq. (38), we obtain the formula for the spectral radiant flux,

$$\frac{[d\mathcal{F}^{(E)}/d\omega_o](t_o)}{\mathcal{F}^{(E)}(0)} = \frac{2}{R^2} \frac{f(r_o)^2}{f(R)} \int_0^{b_{\text{limb}}} \frac{I_e^{(N)}(r_e, \alpha^{-1} \omega_o)}{J_e^{(N)}(R)} \frac{\omega_o}{\langle \omega'_e \rangle|_R} \alpha^2 b \, db. \quad (75)$$

V. NUMERICAL METHOD

As explained previously, in the ray tracing method, worldlines of photons are numerically generated from the observer to the past direction, and the intersection points of the

worldlines of photons and the world sheet of the surface of the star are determined. Then, the observable quantities are calculated from the positions of the intersections. We have made two codes to carry out this procedure, HY's code and KT's code, which are based on fairly different methods. For both codes, we have checked that numerical data reproduce the analytic worldlines of photons for $b = 0$ and $b = b_{\text{crit}}$ discussed in Secs. III A and III B. Also, consistency between the two codes has been checked in situations where the both codes give reliable results.

A. HY's code

As stated before, all of the observable quantities are expressed in terms of the redshift factor α , and the redshift factor α is calculated once the radius r_e and the direction of photon's propagation at the emission event are given. Using this fact, HY's code solves only the radial positions of photons. Differentiating Eq. (25a), we can eliminate b from that equation as

$$\frac{d^2r}{dt^2} + \frac{f^{-1}}{r} \left(1 - \frac{5M}{r}\right) \left(\frac{dr}{dt}\right)^2 = \frac{f}{r} \left(1 - \frac{3M}{r}\right). \quad (76)$$

This equation can be applied for both plus and minus signs of Eq. (25a). In order to handle emission events in the region very close to the horizon with sufficient precision (that is, to calculate extremely small α at the late stage of the collapse), we adopt the tortoise coordinate r_* and solve for $r_*(t)$. The tortoise coordinate is defined by $dr/dr_* = f(r)$, or after integration,

$$r_* = r + 2M \log \left(\frac{r}{M} - 2 \right). \quad (77)$$

In this coordinate, the horizon is located at $r_* = -\infty$, and thus, a sufficient resolution is obtained in the neighborhood of $r = 2M$. Rewriting Eq. (76), the equation for $r_*(t)$ is

$$\frac{d^2r_*}{dt^2} = \frac{1}{r} \left(1 - \frac{3M}{r}\right) \left[1 - \left(\frac{dr_*}{dt}\right)^2\right]. \quad (78)$$

It is easily seen that $r_* = t + \text{const}$ is a solution to this equation. This solution corresponds to the outgoing radial null geodesic given in Eq. (26).

The mass of the star is set to be $M = 1$ in numerical calculations. In solving Eq. (78), the value of r is required for a given r_* . Because the inverse relation of Eq. (77) cannot be given analytically, the relation between r_* and $x := r - 2$ is calculated in advance for discretized

values of $r_* = i \times \Delta r_*$ with $\Delta r_* = 0.01$ for integers i , by solving Eq. (77) with the Newton-Raphson method. If x is smaller than 10^{-15} , the approximate formula $x = \exp(r_*/2 - 1)$ is used. Here, x is chosen rather than r in order to avoid cancellation of significant digits in subtracting two nearly equal numbers. Then, the value of x are generated by the seventh-order Lagrange interpolation for a given r_* .

The equation for $r_*(t)$ is solved using the Runge-Kutta method with the time step $\Delta t = 0.01$ for a given impact parameter b from $t = 0$ to negative time direction, $t = -n\Delta t$ ($n = 1, 2, \dots$). The information of the impact parameter b is included in the “initial condition”, $r = r_o$ and $dr_*/dt = \cos \vartheta_o$ at $t = 0$, where ϑ_o is evaluated by Eq. (38). In this way, we obtain a numerical solution $r_* = p(t)$ for discrete values of t . Because of the time-translational symmetry of the Schwarzschild spacetime, any null geodesic with the same initial conditions except for the arrival time t_o can be obtained just by shifting this solution to the future direction, $r_* = p(t - t_o)$.

Once geodesics are generated numerically, the emission point is calculated for each of the given parameters t_o and b . For this purpose, we generate the data of the world sheet of the star surface in the form $r_* = s(t)$ for discrete moments $t = n'\Delta t$ ($n' = 0, \pm 1, \pm 2, \dots$), using Eqs. (6b) and (6c) for $t \geq t_B$ (before the collapse starts, i.e., for $t < t_B$, the world sheet is chosen to be that of the static star). Using these data, we calculate the distance in the tortoise coordinate between the photon and the star surface, $\mathcal{D} := p(t - t_o) - s(t)$, for each moment of $t = t_o - n\Delta t$ ($n = 0, 1, 2, \dots$). For an interval between two moments in which \mathcal{D} changes its sign, we make an interpolant function of \mathcal{D} , and the equation $\mathcal{D} = 0$ is solved to obtain the emission time t_e and the corresponding tortoise coordinate $r_* = p(t_e)$. Translating from the tortoise coordinate to the circumferential radial coordinate, we obtain the radius r_e of the star surface at the emission event. Then, the redshift factor α are calculated using the formulas (48) and (38). Here, the sign of $\cos \vartheta_e$ must be chosen appropriately as remarked after Eq. (48).

Figure 4 shows the world sheet of the star surface and photons' worldlines with $b/b_{\text{crit}} = 0, 0.1, \dots, 1.3$ and 1.345 in the (r_*, t) -plane that arrive at the point $(r_o, t_o) = (50M, 50M)$ of the observation event. The intersections of geodesics and the world sheet of the star surface are marked by circles (\circ). The photon with $b = 1.345 \times b_{\text{crit}}$ is emitted in an approximately parallel direction to the star surface in the comoving frame during the collapse, and therefore, it initially propagates in the inward direction.

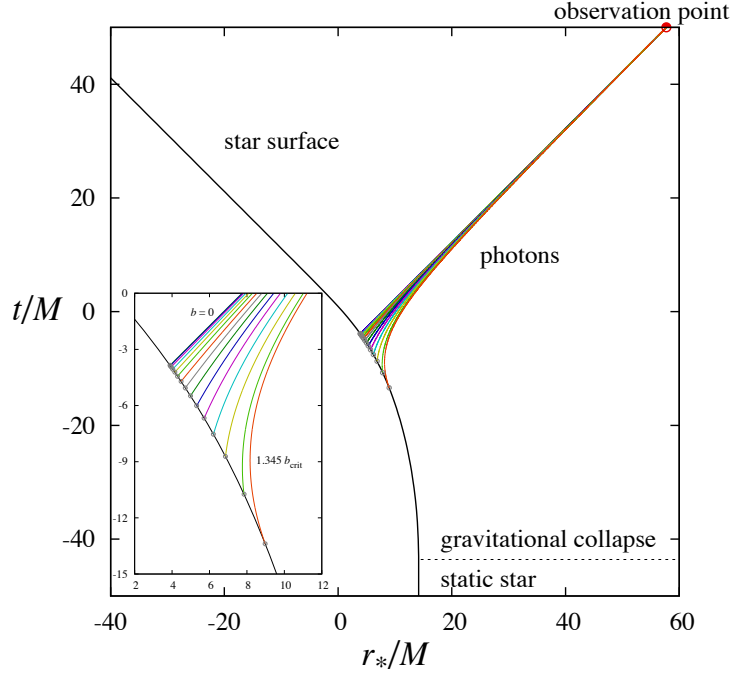


FIG. 4: The world sheet of the star surface and worldlines of photons that arrive at the observer at $(r_o, t_o) = (50M, 50M)$ in the (r_*, t) -plane. The impact parameters of photons are $b/b_{\text{crit}} = 0, 0.1, \dots, 1.3$ and 1.345 , where $b_{\text{crit}} = 3\sqrt{3}M$ is the critical impact parameter. The inset enlarges the emission region.

In order to calculate the observable quantities, we need the dependence of the redshift factor α on the impact parameter b . For this purpose, how to put grid points in the b space is very important, especially at the late stage of the gravitational collapse, because the value of $d\alpha/db$ grows unboundedly large around $b = b_{\text{crit}}$. In order to keep sufficient resolution, we apply the nested grid method in the b space. Namely, we put nine computation domains in the b space, each of which we call the N -th layer with $N = 1, \dots, 9$. The first layer covers the whole range of b and grid points are put as $b = j \times \Delta b^{(1)}$ ($0 \leq j \leq 2151$) with the grid size $\Delta b^{(1)}/b_{\text{crit}} = 10^{-3}$. In each of the N -th layers with $N \geq 2$, five hundred grid points are put as $b = b_{\text{crit}} + j \times \Delta b^{(N)}$ ($-100 \leq j \leq 400$) with $\Delta b^{(N)}/b_{\text{crit}} = 10^{-2-N}$ to give better resolution in the range $1 - 1 \times 10^{-N} \leq b/b_{\text{crit}} \leq 1 + 4 \times 10^{-N}$. In order to proceed with the numerical calculation effectively, not all of the layers are always used: If the N' -th layer is the highest layer in which b_{limb} is included, we use up to the N' -th layer. At an observer's time $t_o = 150M$, up to the ninth layer is necessary. In addition to these layers, the “outer

layer” is put for $2.1400 \leq b/b_{\text{crit}} \leq 2.1516$ with the resolution $\Delta b^{(\text{out})}/b_{\text{crit}} = 10^{-4}$, because a better resolution is required in this domain to correctly describe the behavior of $\alpha(b)$ when the limb of the star image begins shrinking.

There is an upper limit of t_o until which our numerical results are reliable because of the unstable nature of the circular orbit of a photon. Most of the photons observed in the late time have the impact parameter $b \approx b_{\text{crit}}$ and arrive at the observer after orbiting approximately on the photon sphere $r = 3M$. The duration of this orbiting phase becomes longer as t_o is increased. Let us consider a geodesic with the impact parameter precisely equal to b_{crit} . As shown in Eqs. (29)–(32), such a photon asymptotically orbits around the photon sphere $r = 3M$ in the past direction. However, a numerical solution of the same geodesic with $b = b_{\text{crit}}$ finally leaves the photon sphere due to the growth of numerical errors. This gives the upper bound on the duration of the orbiting phase describable by numerical calculations. As a result, our numerical results are reliable up to $t_o \approx 150M$ (for the choice $R = 10M$ and $r_o = 50M$). Beyond this time, a different numerical techniques or an analytic approximate method for asymptotic behavior must be developed (see Sec. VII).

B. KT’s code

In KT’s code, the geodesic equations (23) for $(t(\lambda), r(\lambda), \phi(\lambda))$ are solved on the equatorial plane backward in time using the fourth-order Runge-Kutta method. Here, we would like to note that, unlike HY’s code, not the tortoise coordinate r_* but the circumferential radius r is used as the radial coordinate. The unit of the length is adopted to be M also in this code (i.e., $M = 1$), and the step of the affine parameter is chosen as $\delta\lambda = 10^{-2}$. In KT’s code, geodesics are specified by the value of ϑ_o (rather than b) and they are solved by putting uniform grid points in the ϑ_o space as $\vartheta_o = j \times (\delta\vartheta_o)$ with $\delta\vartheta_o = 6.0 \times 10^{-5}$ for the integers $0 \leq j \leq 5000$. Among them, the geodesics with $0 \leq j \leq 3681$ cross the world sheet of the star surface, whereas the others do not. The “initial” conditions are chosen as $x^\mu = (0, r_o, \pi/2, 0)$ and $k^\mu = (f(r_o)^{-1/2}, f(r_o)^{1/2} \cos \vartheta_o, 0, r_o^{-1} \sin \vartheta_o)$ to generate a null geodesic which arrives at the observer at $t_o = 0$ with the angle ϑ_o . During the numerical calculation, the null condition and the conserved quantities (i.e., the energy and the angular momentum) were monitored to check the accuracy.

The point (t_e, r_e) of an emission event is determined in a different way from HY’s code.

Solving the null geodesic equations, photon's worldline is obtained for discretized values of the affine parameter as $(t(\lambda_n), r(\lambda_n))$, where n is a non-negative integer. Expressing the world sheet of the star surface (6b) and (6c) in the form $t = t_e(r)$, the distance in the time coordinate between the photon and the star surface, $\mathcal{D}' := t(\lambda_n) - t_e(r(\lambda_n))$, is calculated for each n . If \mathcal{D}' changes its sign at $(t(\lambda_n), r(\lambda_n))$, the geodesic equation is solved again forward in time starting from $(t(\lambda_n), r(\lambda_n))$ but with a smaller step of the affine parameter as $\Delta\lambda^{(1)} = \Delta\lambda/4$. Then, within the four steps, \mathcal{D}' changes its sign from negative to positive. Then, again, adopting a further smaller step of the affine parameter as $\Delta\lambda^{(2)} = \Delta\lambda^{(1)}/4$, the geodesic equation is solved backward in time. Iterating these steps, we can obtain fairly accurate value of the intersection point (t_e, r_e) . The redshift factor α is evaluated based on the definitions of the angular frequency, Eqs. (43)–(45).

Because KT's code solves $\phi(\lambda)$ together, it is possible to obtain the orbit in the equatorial plane and the null tangent vector at every point, which are the information that HY's code has discarded. By contrast, due to the use of a uniform grid in the ϑ_o space, the resolution becomes insufficient for $t_o \gtrsim 80M$. Also, because of the use of the circumferential radius r , the coordinate position of the emission event cannot be determined with sufficient accuracy in the neighborhood of the horizon due to cancellation of significant digits. For this reason, basically the data taken by HY's code are shown in the next section. For a figure generated by KT's code, we specify it in caption.

VI. NUMERICAL RESULTS

In this section, we apply our formalism developed in the previous sections to specific examples and present the numerical results for observable quantities. In Secs. VIA–VIC, we discuss the quantities independent of the spectral property of the radiator, i.e., the redshift factor (Sec. VIA), the photon intensity and the radiant intensity (Sec. VIB), and the photon flux and the radiant flux (Sec. VIC). Then, in Sec. VID, we present the results for the spectral photon flux and the spectral radiant flux for the cases of monochromatic and blackbody radiation, one by one. Throughout this section, the initial radius of the star is chosen as $R = 10M$ and the location of the observer as $r_o = 50M$.

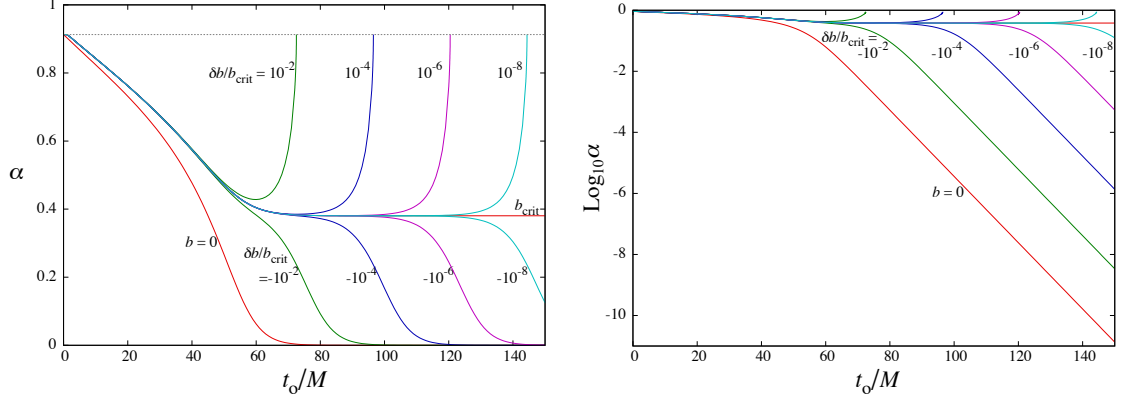


FIG. 5: Left panel: The time evolution of α for fixed impact parameters b in the unit $M = 1$. The cases $b = 0$ and b_{crit} , and $\delta b/b_{\text{crit}} = \pm 10^{-2}, \pm 10^{-4}, \pm 10^{-6}, \pm 10^{-8}$ are shown, where $\delta b := b - b_{\text{crit}}$. Right panel: Same as left panel but the vertical axis is shown in the logarithmic scale.

A. Redshift factor

The left panel of Fig. 5 shows the time evolution of the redshift factor α for fixed values of the impact parameter b , or equivalently, for fixed directions ϑ_o . The cases $b = 0$ and b_{crit} are already shown in Fig. 2, and the same behavior is reproduced by numerical calculation. Additionally, we show the cases $\delta b/b_{\text{crit}} = \pm 10^{-2}, \pm 10^{-4}, \pm 10^{-6}$, and $\pm 10^{-8}$, where

$$\delta b := b - b_{\text{crit}}. \quad (79)$$

For $b > b_{\text{crit}}$, the value of α once decreases, but after some time it begins increasing until it becomes $\alpha = \alpha_{\text{limb}}$. After this moment, α loses its value because the null geodesic does not intersect the world sheet of the star surface. On the other hand, for $b < b_{\text{crit}}$, the value of α continues to decrease to zero, because the intersection of the null geodesic and the world sheet of the star surface, i.e., the emission event, becomes close to the horizon and the effect of the gravitational redshift becomes unlimitedly strong. The right panel of Fig. 5 shows the same figure but the scale of the vertical axis is labeled by $\log_{10} \alpha$. Each curve decays exponentially in time for large t_o . The asymptotic behavior is analytically evaluated as $\propto \exp(-t_o/4M)$ (see the Appendix), and our numerical solutions correspond to this behavior with the error less than 10^{-6} .

Figure 6 shows snapshots of the redshift factor α as functions of the impact parameter b/M . The top left panel shows the cases $t_o/M = 2, 4, \dots, 20$. Initially, the redshift factors of all photons which make the image are identical to α_{limb} defined as Eq. (50). The edge of the

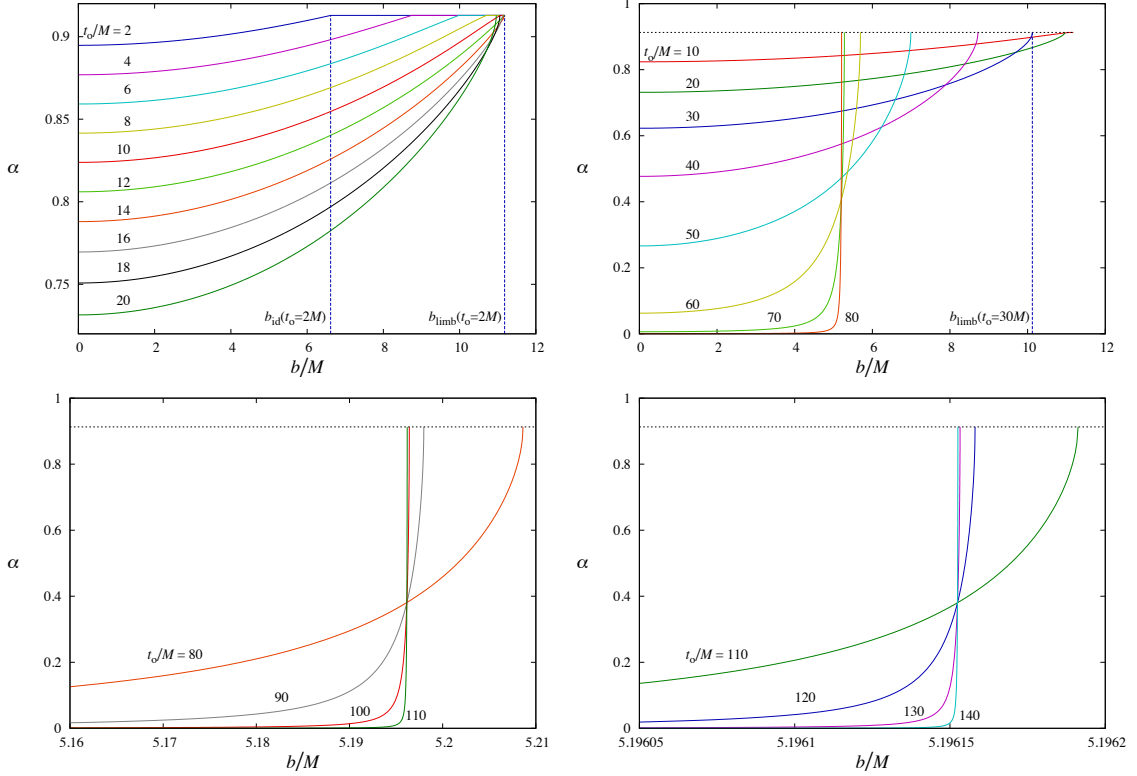


FIG. 6: Snapshots for the redshift factor α of observed photons as a function of the impact parameter b (in the unit $M = 1$). Top left panel: The snapshots for $t_o/M = 2, 4, \dots, 20$. The location of the edge of the inner disk, b_{id} , and the location of the limb, b_{limb} , are shown for $t_o = 2M$. Top right panel: The snapshots for $t_o/M = 10, 20, \dots, 80$. The location of the limb, b_{limb} , is shown for $t_o/M = 30$. Bottom left panel: The snapshots for $t_o/M = 80, 90, 100$, and 110 . Bottom right panel: The snapshots for $t_o/M = 110, 120, 130$, and 140 .

image of the star is made by photons with $b = b_{\text{limb}}(0)$, where $b_{\text{limb}}(0)$ is given by Eq. (56) ($5\sqrt{5}M$ in our parameter choice).

After the collapse begins, the redshift factor begins decreasing in a portion of the image with $0 \leq b \leq b_{\text{id}}$, which corresponds to the “inner disk” $0 \leq \vartheta_o \leq \vartheta_o^{(\text{id})}$ in the image, where $b_{\text{id}} = 0$ for $t_o \leq 0$ and $0 < b_{\text{id}} \leq b_{\text{limb}}$ for $t_o > 0$. In this portion, the redshift factor α takes values $\alpha_{\text{cent}} \leq \alpha \leq \alpha_{\text{limb}}$, where α_{cent} is defined in Eq. (51). Outside the inner disk, there is a region $b_{\text{id}} \leq b \leq b_{\text{limb}}(0)$ with a constant redshift factor α_{limb} . The inner disk grows bigger as time goes on, and at $t_o = t_o^{(\text{full})}$, it fulfills the whole image.

The value of $t_o^{(\text{full})}$ is determined as follows. Consider a null geodesic with the impact parameter $b = b_{\text{limb}}(0)$ that passes through the point (t_o, r_o) of the observation event. In

the period $0 \leq t_o < t_o^{(\text{full})}$, this null geodesic is tangent to the world sheet of the static star surface at the point where they intersect, since the star is before the beginning of the collapse at the emission event of the corresponding photon, i.e., (t_e, R) with $t_e < 0$. By contrast, in the period $t_o^{(\text{full})} < t_o$, the null geodesic with $b = b_{\text{limb}}(0)$ and the world sheet of the star surface no longer intersect each other. Therefore, $t_o^{(\text{full})}$ is the observer's time such that this null geodesic becomes tangent to the world sheet of the star surface precisely at the point (t_e, R) with $t_e = 0$, i.e., just when the star begins the gravitational collapse. By studying this condition numerically, we have found $t_o^{(\text{full})}/M \approx 11.8887$.

The top right and bottom two panels of Fig. 6 shows the behavior of $\alpha(b)$ for $t_o/M = 10, 20, \dots, 140$. In the top right panel, the location of b_{limb} is also shown for $t_o/M = 30$. In the central region, the redshift factor decays rapidly to zero. Throughout the collapse, the redshift factor α_{cent} at the central point $b = 0$ takes the minimum value. The behavior of $\alpha(b)$ around the central point $b = 0$ can be perturbatively studied as presented in the Appendix.

The value of b_{limb} is time dependent for $t > t_o^{(\text{full})}$. It decreases in time and asymptotes to b_{crit} . The redshift factor α_{limb} at the limb is unchanged throughout the collapse. Note, however, that the derivative $\partial\alpha/\partial b$ diverges there for $t_o > t_o^{(\text{full})}$ for the following reason. Let us express worldlines of photons with the impact parameters b that pass through the observation point (t_o, r_o) as $t = t^{(t_o, r_o)}(r, b)$. In order to consider the intersection with the world sheet of the star surface, we substitute $t = t_e$ and $r = r_e$ into this formula. Since t_e is a function of r_e through Eqs. (6b) and (6c), we have the equation for r_e as

$$t_e(r_e) = t^{(t_o, r_o)}(r_e, b). \quad (80)$$

By solving this equation with respect to r_e , we have the radius r_e of the emission event as a function of b for fixed values of (t_o, r_o) , i.e., $r_e = r_e^{(t_o, r_o)}(b)$. Differentiating Eq. (80) with respect to b , we find

$$\frac{dr_e}{db} = \frac{\left. \frac{\partial t^{(t_o, r_o)}}{\partial b} \right|_{r=r_e}}{\left. \frac{dt_e}{dr_e} - \frac{\partial t^{(t_o, r_o)}}{\partial r} \right|_{r=r_e}}. \quad (81)$$

The worldline of a photon with b_{limb} becomes tangential to the world sheet of the star surface at the emission event $r = r_e$ in the (r, t) -plane (see Fig. 4), and this means that the denominator of Eq. (81) becomes zero. Therefore, dr_e/db becomes infinity at $b = b_{\text{limb}}$.

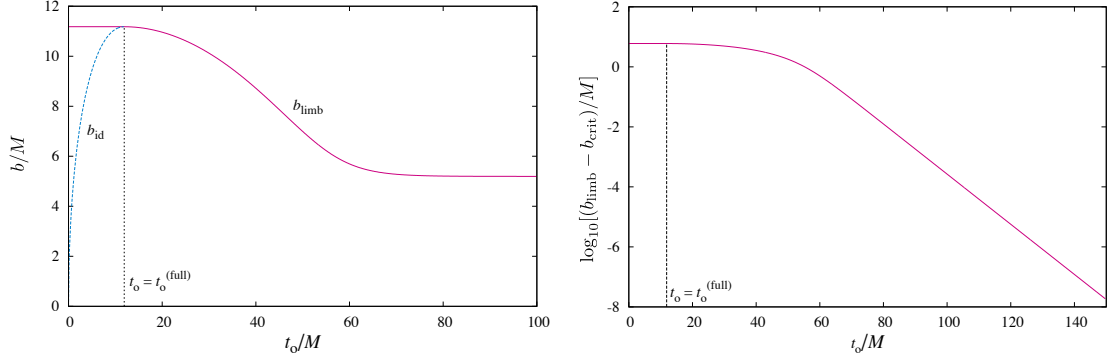


FIG. 7: Left panel: The impact parameters at the limb and at the edge of the inner disk, b_{limb}/M and b_{id}/M respectively, as functions of t_o/M . Right panel: The difference of b_{limb} from the critical impact parameter $b_{\text{crit}} = 3\sqrt{3}M$ (shown in the logarithmic scale, $\log_{10}[(b_{\text{limb}} - b_{\text{crit}})/M]$) as a function of t_o/M .

Since the redshift factor α is given as a function of r_e as discussed before and it can be checked that $d\alpha/dr_e$ is nonvanishing, the value of $\partial\alpha/\partial b$ also diverges.

The function $\alpha(b)$ becomes steeper near $b = b_{\text{crit}}$ as t_o is increased. In the bottom two panels, all curves approximately intersect at a point $(b, \alpha) = (b_{\text{crit}}, \alpha_\infty)$, where α_∞ is defined as Eq. (53). For late time, $\alpha(b)$ shrinks exponentially in time in the direction of b with respect to b_{crit} .

The left panel of Figure 7 shows the behavior of b_{id} and b_{limb} as functions of the observer's time. For $0 \leq t_o \leq t_o^{(\text{full})}$, b_{limb} is unchanged. b_{id} is an increasing function and merges with the line of b_{limb} at $t_o = t_o^{(\text{full})}$. For $t_o > t_o^{(\text{full})}$, b_{limb} is dependent on an observer's time t_o . It decreases and asymptotes to b_{crit} . Correspondingly, the limb of the star image asymptotes to

$$\sin \vartheta_o^{(\text{limb})}(\infty) = \frac{3\sqrt{3f(r_o)}}{r_o}M, \quad (82)$$

from Eq. (38). The right panel shows the value of $\log_{10}[(b_{\text{limb}} - b_{\text{crit}})/M]$ as a function of the observer's time. The asymptotic behavior is numerically evaluated as $b_{\text{limb}} - b_{\text{crit}} \approx 0.000266 \times M \exp[-0.192449 \times (t_o/M - 100)]$. An approximate late time analysis in Sec. VII will show $b_{\text{limb}} - b_{\text{crit}} \propto \exp[-t_o/3\sqrt{3}M]$, and our numerical data agree well with this behavior.

Figure 8 presents a picture that mimics images of the star obtained through a telescope at four moments: The first, second, third and forth quadrants are for $t_o/M = 0, 30, 50,$

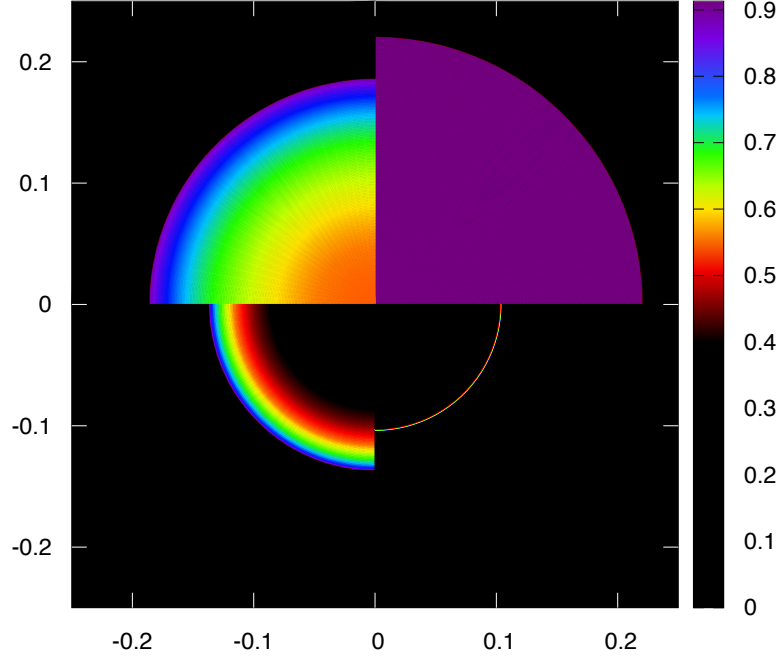


FIG. 8: Images of the star (with redshift factor indicated by color online) for $t_o = 0, 35, 50$, and 69 (counterclockwise from top right). These images have been generated by KT's code.

and 69 , respectively. In the online version of this paper, Fig. 8 is shown by color, and the color is chosen to be consistent with the case where the star surface emits near ultraviolet monochromatic radiation of the wavelength $\lambda \sim 353$ nm. Initially, photons experience only gravitational redshift, and the whole star image is uniformly purple as shown in the first quadrant. After the collapse begin, a red domain appears near the center as the second quadrant, and as time goes on, arriving photons near the center become infrared. Because infrared photons are invisible to human eyes, such a domain is shown by black in the third and fourth quadrants. After that, the wavelength of arriving photons near the central region grows unlimitedly large with the observer's time. By contrast, in the neighborhood of the limb, photons remain visible, showing rainbow colors around $t_o = 50M$ in the third quadrant. As t_o is increased, the star image becomes very thin as the fourth quadrant and arriving photons typically have the wavelength around that of yellow color (i.e. $\lambda \sim 600$ nm). The wavelength at the limb $\vartheta_o = \vartheta_o^{(\text{limb})}$ is unchanged from purple color throughout the collapse.

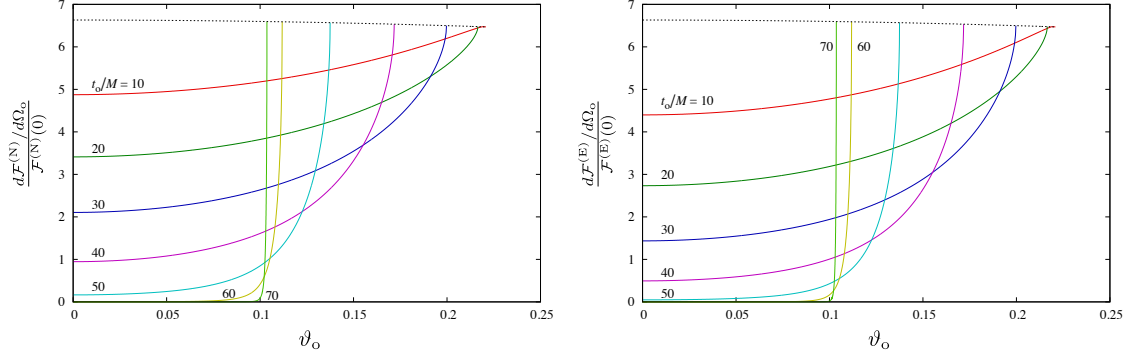


FIG. 9: Snapshots of the photon intensity (left panel) and the radiant intensity (right panel) as functions of the observation direction ϑ_o for $t_o/M = 0$ (dotted curves), and $t_o/M = 10, 20, \dots, 70$ (solid curves).

Note that although this figure correctly represents color, the surface brightness is not very accurate. The study on the spectral radiant flux in Sec. VID 1 will show that the rainbow colored region is darker compared to Fig. 8 in reality.

B. Photon and radiant intensity

If the radiator's spectral photon intensity in the comoving frame does not depend on time as assumed in Secs. II B 1 and II B 2, the photon intensity (63) and the radiant intensity (73) do not depend on the angular frequency spectrum of the radiator because $J_e^{(N)}(r_e) = J_e^{(N)}(R)$ and $\langle \omega'_e \rangle|_{r_e} = \langle \omega'_e \rangle|_R$ hold throughout the collapse. Here, we show the numerical results of the observed intensities in this case.

The left and right panels of Fig. 9 show snapshots of the photon intensity and the radiant intensity, respectively, as functions of the angle ϑ_o . The cases of $t_o/M = 0, 10, \dots, 70$ are depicted. From this figure, we see that the values of the two kinds of intensity at the limb slightly changes during the collapse due to the factor of $\cos \vartheta_o$ in Eqs. (63) and (73). In the central region, the photon intensity and the radiant intensity rapidly decrease as $\sim \exp[-(3/4M)t_o]$ and $\sim \exp[-t_o/M]$, because they are proportional to α^3 and α^4 , respectively. To our eyes, only the neighborhood of the limb of the apparent disk seems to be shining like a ring, and the ring becomes thinner and thinner as time goes on.

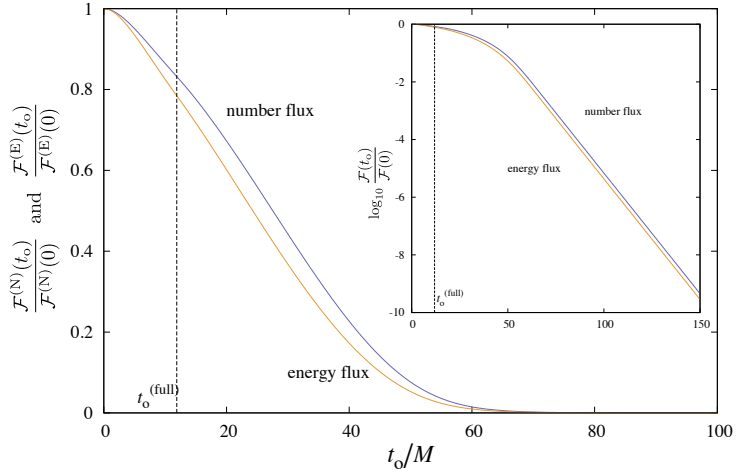


FIG. 10: Normalized photon flux $\mathcal{F}^{(N)}(t_o)/\mathcal{F}^{(N)}(0)$ and normalized radiant flux $\mathcal{F}^{(E)}(t_o)/\mathcal{F}^{(E)}(0)$ as functions of the observation time t_o/M .

C. Photon and radiant fluxes

Figure 10 shows the behavior of the photon flux (64) and the radiant flux (74) as functions of the observer's time t_o/M . The photon flux and the radiant flux are monotonically decreasing functions. The radiant flux decays faster than the photon flux due to the difference in the power, α^4 and α^3 , in the integrand of Eqs. (64) and (74). The inset shows the same functions but the vertical axis is shown in the logarithmic scale. The photon flux and the radiant flux decay exponentially for large t_o as $\mathcal{F}(t_o)/\mathcal{F}(0) \approx \hat{\mathcal{F}}_{100} \exp[-\gamma(t_o/M - 100)]$. Here, $\hat{\mathcal{F}}_{100} = 6.858 \times 10^{-6}$ and $\gamma = 0.192451$ for the photon flux, and $\hat{\mathcal{F}}_{100} = 4.308 \times 10^{-6}$ and $\gamma = 0.192454$ for the radiant flux. These are consistent with the asymptotic behavior $\propto \exp[-t_o/3\sqrt{3}M]$, which has already been derived by Ames and Thorne [10].

D. Spectral photon and radiant fluxes

Here, we show the numerical results of the spectral photon flux and the spectral radiant flux. Since these quantities depend on the spectral property of the radiator, we discuss the cases of monochromatic radiation and blackbody radiation separately.

1. The case of monochromatic radiation

In the case of monochromatic radiation whose spectral radiance is given by the delta-functional form, Eq. (15), the integration in the formulas for the spectral photon flux and the spectral radiant flux, Eqs. (67) and (75), cannot be done numerically. For this reason, we rewrite these formulas to make them tractable with numerical calculations. If we normalize the observed angular frequency ω_o with the angular frequency $\bar{\omega}'_e$ at the emission event, it corresponds to the redshift factor as $\alpha = \omega_o/\bar{\omega}'_e$. For this reason, we calculate $d\mathcal{F}^{(N)}/d\alpha = \bar{\omega}'_e d\mathcal{F}^{(N)}/d\omega_o$ and $d\mathcal{F}^{(E)}/d\alpha = \bar{\omega}'_e d\mathcal{F}^{(E)}/d\omega_o$ as functions of α .

For $0 \leq t_o \leq t_o^{(\text{full})}$, it is convenient to divide the integration domain into two parts, the first one for $0 \leq b \leq b_{\text{id}}$ and the second one for $b_{\text{id}} \leq b \leq b_{\text{limb}}$. The second integral is easy because in this region, the argument of the delta function $\delta(\omega_o/\alpha - \bar{\omega}'_e)$ does not depend on b . In order to proceed with the first integral, we consider the inverse relation of $\alpha = \alpha(b, t_o)$ for a fixed t_o , i.e., $b = b(\alpha, t_o)$ and rewrite the integral as the one with respect to α . Since $\delta(\omega_o/\alpha - \bar{\omega}'_e) = (\alpha^2/\omega_o)\delta(\alpha - \omega_o/\bar{\omega}'_e)$ holds, we obtain

$$\hat{\mathcal{F}}_\alpha^{(N)}(t_o) := \frac{d\mathcal{F}^{(N)}/d\alpha}{\mathcal{F}^{(N)}(0)} = \frac{2}{R^2} \sqrt{\frac{f(r_o)^3}{f(R)}} \frac{J_e^{(N)}(r_e)}{J_e^{(N)}(R)} \alpha^3 b \frac{db}{d\alpha} + \left(1 - \frac{b_{\text{id}}^2}{b_{\text{limb}}^2}\right) \delta(\alpha - \alpha_{\text{limb}}), \quad (83a)$$

$$\hat{\mathcal{F}}_\alpha^{(E)}(t_o) := \frac{d\mathcal{F}^{(E)}/d\alpha}{\mathcal{F}^{(E)}(0)} = \frac{2}{R^2} \frac{f(r_o)^2}{f(R)} \frac{J_e^{(N)}(r_e)}{J_e^{(N)}(R)} \frac{\langle \omega'_e \rangle|_{r_e}}{\langle \omega'_e \rangle|_R} \alpha^4 b \frac{db}{d\alpha} + \left(1 - \frac{b_{\text{id}}^2}{b_{\text{limb}}^2}\right) \delta(\alpha - \alpha_{\text{limb}}), \quad (83b)$$

after integration, with the constraint $\alpha = \omega_o/\bar{\omega}'_e$. Remember that α_{limb} in the second term is the initial redshift factor defined in Eq. (50). The formula for $t_o \geq t_o^{(\text{full})}$ is obtained by omitting the second term. Note that by virtue of Eq. (16), the formulas (83a) and (83b) are further simplified because $J_e^{(N)}(r_e) = J_e^{(N)}(R)$ and $\langle \omega'_e \rangle|_{r_e} = \langle \omega'_e \rangle|_R$ hold. We also remark that the first terms of Eqs. (83a) and (83b) can be derived from the formulas for the photon intensity (63) and the radiant intensity (73) just by rewriting ϑ_o with α , because there is one to one correspondence between ϑ_o and α for a fixed t_o .

Top left and top right panels of Fig. 11 show snapshots of $\hat{\mathcal{F}}_\alpha^{(N)}$ as a function of α for the moments $t_o/M = 0, 2, \dots, 20$ and $t_o/M = 20, 30, \dots, 70$, respectively. Because we cannot plot the delta-functional profile, only the first term of Eqs. (83a) is shown. The range where the values of $\hat{\mathcal{F}}_\alpha^{(N)}$ is nonzero is limited within $\alpha_{\text{cent}} \leq \alpha \leq \alpha_{\text{limb}}$, where α_{cent} is defined as Eq. (51) and is regarded as a function of only the observer's time t_o . When t_o is small, $\hat{\mathcal{F}}_\alpha^{(N)}$ is a monotonically increasing function of α . But the value of $\hat{\mathcal{F}}_\alpha^{(N)}$ at the limb $\alpha = \alpha_{\text{limb}}$

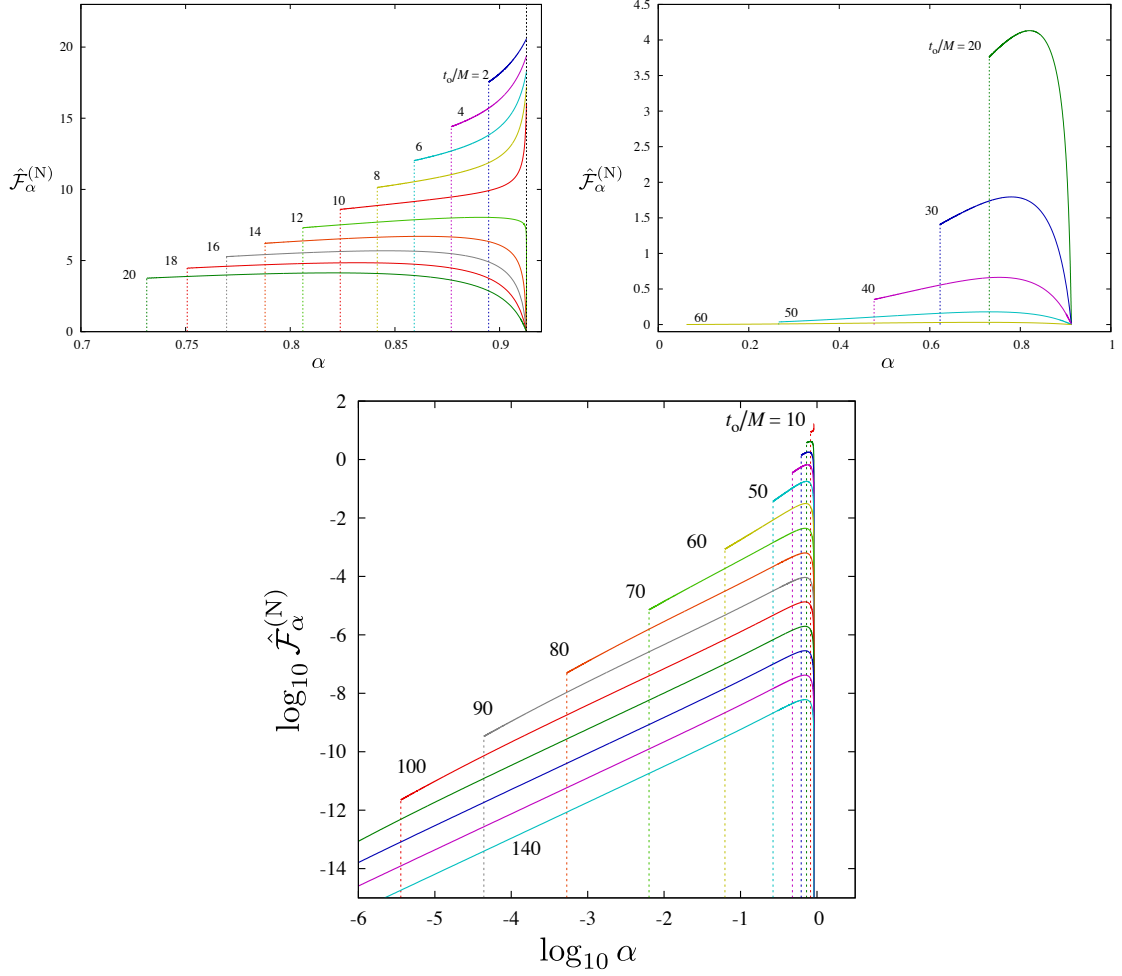


FIG. 11: Snapshots of the normalized spectral photon flux $\hat{\mathcal{F}}_\alpha^{(N)}$ as a function of $\alpha := \omega_o/\bar{\omega}'_e$ for the case of monochromatic radiator. Here, only the first terms of Eq. (83a) is shown. Top left panel: Snapshots for $t_o/M = 2, 4, \dots, 20$. Top right panel: Snapshots for $t_o/M = 20, 30, \dots, 60$. Bottom panel: Snapshots for $t_o/M = 10, 20, \dots, 140$, where horizontal and vertical axes are shown in the logarithmic scale.

decreases because at the edge $b = b_{\text{id}}$ of the inner disk $0 \leq b \leq b_{\text{id}}$, the value of $d\alpha/db$ grows larger as time goes on (see Fig. 6) and becomes infinity after the edge arrives at the limb of the image, i.e., $t_o > t_o^{(\text{full})}$. As a result, $\hat{\mathcal{F}}_\alpha^{(N)}$ is always zero at $\alpha = \alpha_{\text{limb}}$ for $t_o > t_o^{(\text{full})}$. Since $\hat{\mathcal{F}}_\alpha^{(N)}$ is an increasing function in the neighborhood of $\alpha = \alpha_{\text{cent}}$ (see the Appendix for an analytic explanation), a peak appears for $t_o > t_o^{(\text{full})}$. The bottom panel of Fig. 11 shows the relation between $\hat{\mathcal{F}}_\alpha^{(N)}$ and α , but both axes are shown in the logarithmic scale. It can be seen that for late time, the curve approximately keeps its shape and size (except for the

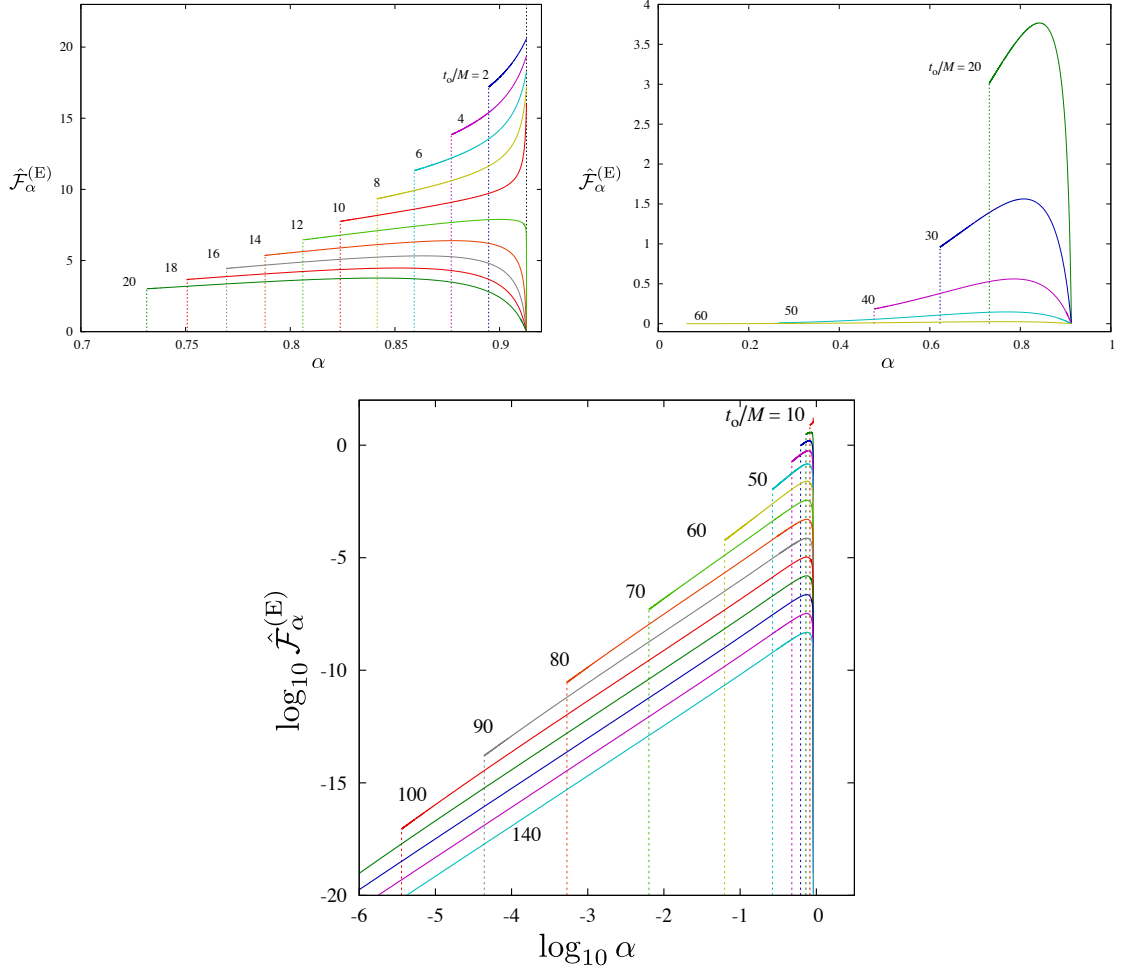


FIG. 12: Same as Fig. 11 but for the (normalized) spectral radiant flux $\hat{\mathcal{F}}_\alpha^{(E)}$. Here, only the first term of Eq. (83b) is shown.

region of very small $\alpha \sim \alpha_{\text{cent}}$) and shifts down in a parallel manner as t_o is increased. This means that the spectral photon flux decays exponentially in time. $\hat{\mathcal{F}}_\alpha^{(N)}$ is approximately proportional to α in small region of α , and there remains a peak in the spectrum. The asymptotic position of the peak is $\alpha \approx 0.69638$, and it is consistent with $\alpha \approx 0.69625$ that will be derived in the asymptotic analysis in the next section. Our results indicate that the redshift factor of most of the arriving photons from the star remains finite, and a star becomes invisible because the rate of photon detection becomes slower.

Figure 12 is the same as Fig. 11 but for the spectral radiant flux, $\hat{\mathcal{F}}_\alpha^{(E)}$. Qualitatively similar behavior to the spectral photon flux $\hat{\mathcal{F}}_\alpha^{(N)}$ is observed. For late time, $\hat{\mathcal{F}}_\alpha^{(E)}$ is approximately proportional to α^2 in small region of α , and a peak remains in the spectrum. The

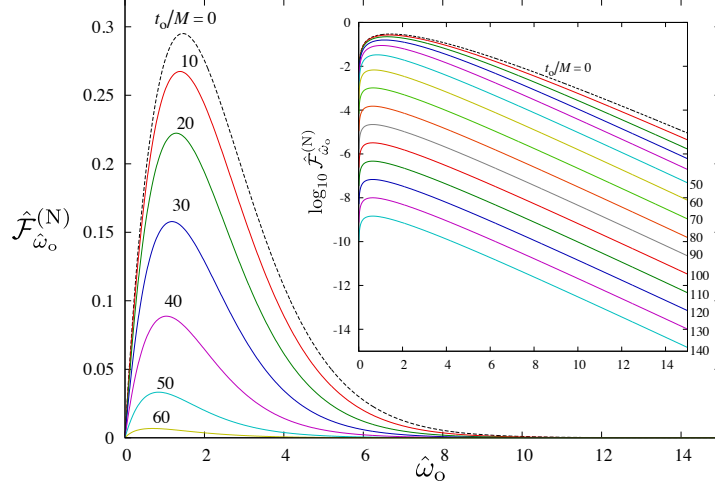


FIG. 13: Snapshots of the normalized spectral photon flux $\hat{\mathcal{F}}_{\hat{\omega}_o}^{(N)}$ as a function of $\hat{\omega}_o := \omega_o/T'_e$ for the case of blackbody radiator for $t_o/M = 10, 20, \dots, 60$. The inset shows snapshots for $t_o/M = 10, 20, \dots, 140$, where the vertical axis is shown in the logarithmic scale.

asymptotic position of the peak is $\alpha \approx 0.74948$, and it is consistent with $\alpha \approx 0.74944$ that will be derived in the asymptotic analysis in the next section. The bottom panel plots the same relation as Fig. 3 by Ames and Thorne [10]. Here, we have presented the “modern version” generated by huge power of a recent computer.

2. The case of blackbody radiation

Now, we turn our attention to the case of blackbody radiation with constant temperature given by Eqs. (17)–(19). Since the star surface emits photons with typical angular frequency $\omega'_e \sim T'_e$, it is convenient to normalize the observed angular frequency as $\hat{\omega}_o := \omega_o/T'_e$. In terms of $\hat{\omega}_o$, the spectral formulas (67) and (75) become

$$\hat{\mathcal{F}}_{\hat{\omega}_o}^{(N)}(t_o) = \frac{d\mathcal{F}^{(N)}/d\hat{\omega}_o}{\mathcal{F}^{(N)}(0)} = \frac{\zeta(3)^{-1}}{R^2} \sqrt{\frac{f(r_o)^3}{f(R)}} \hat{\omega}_o^2 I(\hat{\omega}_o), \quad (84a)$$

$$\hat{\mathcal{F}}_{\hat{\omega}_o}^{(E)}(t_o) = \frac{d\mathcal{F}^{(N)}/d\hat{\omega}_o}{\mathcal{F}^{(N)}(0)} = \frac{30/\pi^4}{R^2} \frac{f(r_o)^2}{f(R)} \hat{\omega}_o^3 I(\hat{\omega}_o), \quad (84b)$$

where

$$I(\hat{\omega}_o) := \int_0^{b_{\text{limb}}} \frac{bdb}{\exp(\hat{\omega}_o/\alpha) - 1} \quad (85)$$

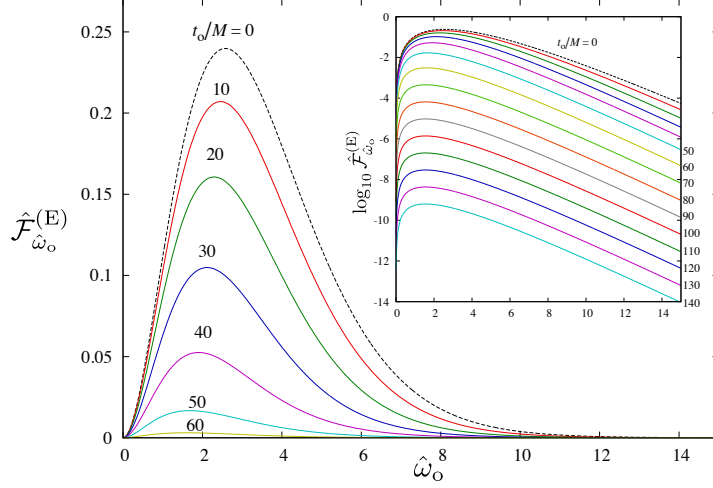


FIG. 14: Same as Fig. 13 but for the normalized spectral radiant flux $\hat{\mathcal{F}}_{\hat{\omega}_o}^{(E)}$.

Figures 13 and 14 show snapshots of $\hat{\mathcal{F}}_{\hat{\omega}_o}^{(N)}$ and $\hat{\mathcal{F}}_{\hat{\omega}_o}^{(E)}$, respectively, as functions of $\hat{\omega}_o$ for the moments $t_o/M = 0, 10, \dots, 60$. The inset of each figure shows the moments $t_o/M = 0, 10, \dots, 140$ but the vertical axis is shown in the logarithmic scale. Throughout the evolution, each of the two curves, $\hat{\mathcal{F}}_{\hat{\omega}_o}^{(N)}$ and $\hat{\mathcal{F}}_{\hat{\omega}_o}^{(E)}$, has a peak throughout the evolution. Initially, the peak locations are $\hat{\omega}_o \approx 1.455$ and ≈ 2.576 , respectively. The location of each peak shifts toward a smaller value of $\hat{\omega}_o$ a bit, but remains a nonzero finite value. The asymptotic peak location is $\hat{\omega}_o \approx 0.63973$ and 1.55367 for $\hat{\mathcal{F}}_{\hat{\omega}_o}^{(N)}$ and $\hat{\mathcal{F}}_{\hat{\omega}_o}^{(E)}$, respectively. The shapes of $\log_{10} \hat{\mathcal{F}}_{\hat{\omega}_o}^{(N)}$ and $\log_{10} \hat{\mathcal{F}}_{\hat{\omega}_o}^{(E)}$ scarcely change, and the curves shift to the lower direction. This means that $\hat{\mathcal{F}}_{\hat{\omega}_o}^{(N)}$ and $\hat{\mathcal{F}}_{\hat{\omega}_o}^{(E)}$ decay exponentially in time. Similarly to the case of monochromatic radiation, a star becomes invisible because the rate of photon detection becomes lower.

The photon number spectrum $dN/d\omega_o$ and energy spectrum $dE/d\omega_o$ (in the period $t_o \geq 0$) are obtained by integrating the spectral flux $d\mathcal{F}^{(N)}/d\omega_o$ and $d\mathcal{F}^{(E)}/d\omega_o$ with respect to the observer's proper time $\tau_o = \sqrt{f(r_o)}t_o$. As nondimensional quantities, we calculate

$$\hat{\mathcal{N}}_{\hat{\omega}_o} := \frac{\sqrt{f(r_o)}}{M} \int_0^{t_o^{(\text{cut})}} \hat{\mathcal{F}}_{\hat{\omega}_o}^{(N)} dt_o, \quad (86)$$

$$\hat{\mathcal{E}}_{\hat{\omega}_o} := \frac{\sqrt{f(r_o)}}{M} \int_0^{t_o^{(\text{cut})}} \hat{\mathcal{F}}_{\hat{\omega}_o}^{(E)} dt_o, \quad (87)$$

where $t_o^{(\text{cut})}$ indicates an upper cutoff value of the integration domain, which we choose $t_o^{(\text{cut})} = 150M$. Solid curves of Fig. 15 show these quantities as functions of $\hat{\omega}_o$. For comparison, the rescaled initial values of the two kinds of flux, $30.43 \times \hat{\mathcal{F}}_{\hat{\omega}_o}^{(N)}$ and $26.87 \times \hat{\mathcal{F}}_{\hat{\omega}_o}^{(E)}$, are shown by

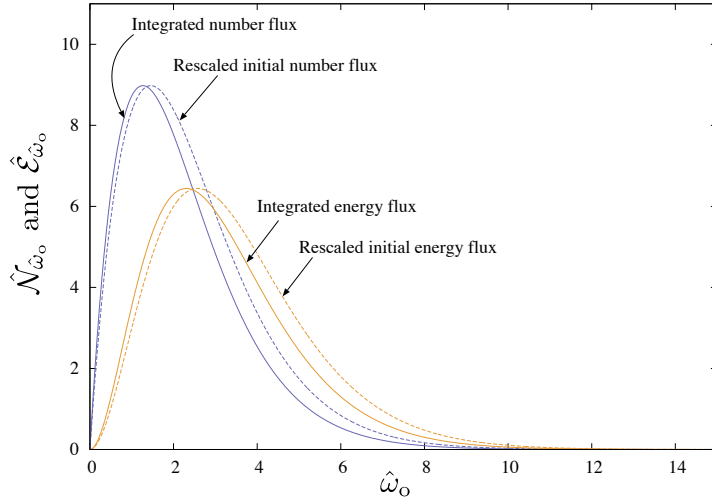


FIG. 15: Photon number spectrum $\hat{\mathcal{N}}_{\hat{\omega}_o}$ and energy spectrum $\hat{\mathcal{E}}_{\hat{\omega}_o}$ as functions of $\hat{\omega}_o := \omega_o/T'_e$ integrated in the period $0 \leq t_o/M \leq 150$.

dashed curves. The photon number spectrum and the radiant energy spectrum have peaks at $\hat{\omega}_o \approx 1.265$ and $\hat{\omega}_o \approx 2.303$, respectively. Compared to the peak positions of two kinds of initial flux, $\hat{\omega}_o \approx 1.455$ and $\hat{\omega}_o \approx 2.576$, the peak positions shift toward smaller values of $\hat{\omega}_o$.

VII. APPROXIMATE ANALYSIS ON ASYMPTOTIC BEHAVIOR

In our numerical results, as t_o is increased, each of the two kinds of spectral flux asymptotes to a configuration with a peak at some fixed value of angular frequency, and its magnitude decays exponentially with time t_o . In this section, we develop a new approximate method to give analytic formulas for late time behavior.

A. Method

The primary contribution to the spectral photon and radiant flux for the late time behavior comes from photons with the impact parameter b close to the critical value b_{crit} . Hence, we study the approximate behavior for worldlines of photons for small δb compared to M , where δb is defined as Eq. (79). Our first trial was to treat the deviation from the worldline of a photon with $b = b_{\text{crit}}$, which is given analytically as Eqs. (30)–(32), as a perturbation. However, although we can obtain an analytic formula for the perturbative quantity as well,

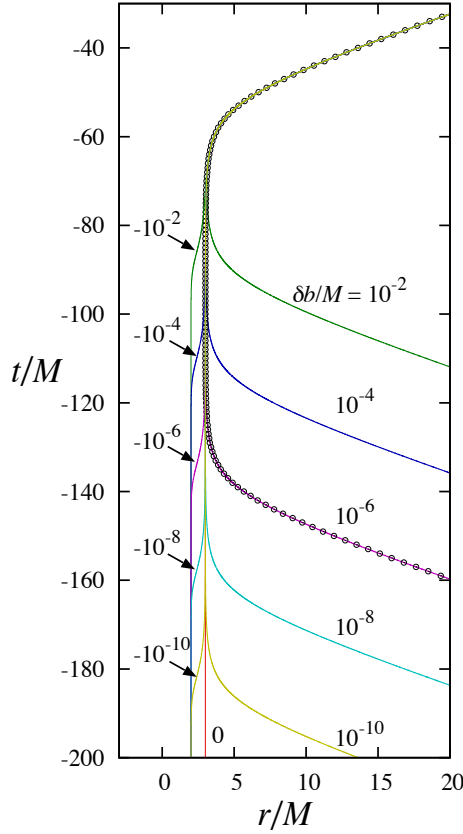


FIG. 16: Worldlines of photons with impact parameters $\delta b/M = 0, \pm 10^{-2}, \pm 10^{-4}, \pm 10^{-6}, \pm 10^{-8}$, and $\pm 10^{-10}$ that pass through the observation point $t_o = 0$ and $r_o = 50M$. Here, δb is defined by $\delta b := b - b_{\text{crit}}$. Except for the case $\delta b = 0$, numerically generated data are shown. For the case of $\delta b/M = 10^{-6}$, the worldline obtained by the approximate formula (88) is shown by circles (\odot). The approximate worldline coincides with the numerical one very well.

it includes a strongly divergent term proportional to $(r - 3M)^{-2}$. Therefore, the perturbative scheme breaks down in the vicinity of the photon sphere, $|r - 3M| \lesssim \sqrt{M\delta b}$.

Instead of perturbation, we develop a method of nonperturbative approximation here. Before doing this, let us look at worldlines of photons with $|\delta b/M| \ll 1$. Since a worldline with $\delta b > 0$ has a turning point in general (a pericenter in the case of a worldline in the region $r > 3M$), it is convenient to regard r as a function of t in order to describe it, because $r(t)$ becomes a single-valued function. The equation for $r(t)$ is given by Eq. (76). Figure 16 shows the worldlines of photons with $\delta b/M = 0, \pm 10^{-2}, \pm 10^{-4}, \pm 10^{-6}, \pm 10^{-8}$, and $\pm 10^{-10}$ that pass through the point $(t_o, r_o) = (0, 50M)$. The photon motion has three phases: (i)

Approaching phase where a photon with $\delta b > 0$ (respectively, $\delta b < 0$) becomes closer to the photon sphere $r = 3M$ from the outside (respectively, inside) region; (ii) *Orbiting phase* where the photon orbits approximately on the photon sphere; and (iii) *Escaping phase* where the photon leaves the photon sphere and propagates to the observer. As $|\delta b/M|$ becomes smaller, duration of the orbiting phase becomes longer. The worldline in the escaping phase is approximately the same as that of $b = b_{\text{crit}}$, with the error of $O(\delta b/M)$. Since the worldline of the approaching phase for $\delta b > 0$ is just the time reversal of the escaping phase, it also can be approximated in the same manner. For $\delta b < 0$, it is possible to approximate its worldline with an analytic formula of the photon worldline with $b = b_{\text{crit}}$ that approaches the photon sphere from the inside of the photon sphere (see below).

These observations lead to the following approximate method. First, we consider the case $\delta b > 0$. We introduce a function $r - 3M = \tilde{F}(t)$ that is equivalent to the analytic worldline $t = F^{(\text{out})}(r)$ of an outwardly propagating photon with the critical impact parameter b_{crit} , where $F^{(\text{out})}(r)$ is given by Eq. (32) with Eqs. (30) and (31). For a later convenience, we introduce $G(r) := -F^{(\text{out})}(r)$. As mentioned in Sec. III B, $t = G(r)$ describes a worldline of a photon with the critical impact parameter b_{crit} that asymptotes to the photon sphere $r = 3M$ from the outside region. We introduce a function $r - 3M = \tilde{G}(t)$ that is equivalent to $t = G(r)$. Then, these two solutions are combined as

$$r - 3M = \tilde{F}(t - t_o + F^{(\text{out})}(r_o)) + \tilde{G}(t + D). \quad (88)$$

to approximate the worldline with $\delta b > 0$. Here, D is a parameter related to the length of the orbiting phase that will be related to the value of the impact parameter δb .

The formula (88) actually gives an approximate worldline in the following sense. In the escaping (respectively, approaching) phase, the second term $\tilde{G}(t + D)$ [respectively, the first term $\tilde{F}(t - t_o + F^{(\text{out})}(r_o))$] is exponentially small and approximately zero. Thus, the formula approximately satisfies Eq. (76). In the orbiting phase, the formula (88) gives a correct perturbative behavior from $r = 3M$. Introducing $\delta r := r - 3M$, Eq. (76) is linearized as

$$\frac{d^2}{dt^2} \delta r = \frac{1}{27M^2} \delta r. \quad (89)$$

The formula (88) approximately behaves as

$$\frac{r}{M} - 3 \approx \exp \left[\frac{t - t_o - C + F^{(\text{out})}(r_o)}{3\sqrt{3}M} \right] + \sigma \exp \left[-\frac{t + C + D}{3\sqrt{3}M} \right], \quad (90)$$

with $\sigma = +1$ in the orbiting phase, which satisfies the perturbative equation (89). Here, C is defined by Eq. (36).

Now, we relate D with δb . From Eq. (25a), the radial coordinate $r = r_p$ of the pericenter of the photon worldline is determined by the equation $r^2 = b^2 f$, and it is perturbatively solved as $r_p/M - 3 = (4/3)^{1/4}(\delta b/M)^{1/2} + O(\delta b/M)$. By contrast, the minimum value of the right-hand side of Eq. (90) is $\exp\left[\frac{(-t_o + F^{(\text{out})}(r_o) - D)/2 - C}{3\sqrt{3}M}\right]$. Equating these two, we have

$$D = -t_o + F^{(\text{out})}(r_o) - 2C - 3\sqrt{3}M \log\left|\frac{\delta b}{M}\right| + \frac{3\sqrt{3}}{2}(\log 12)M. \quad (91)$$

Since this perturbative quantity is $O(\sqrt{\delta b/M})$ in the orbiting phase, the error in this approximation is $O(\delta b/M)$ in all phases. In Fig. 16, the behavior of the approximate formula (88) with (91) is shown by circles for $\delta b/M = 10^{-6}$ and is compared with the numerical solution. The approximate formula remarkably coincides with the numerical solution. If a photon is emitted from the point $(t, r) = (t_e, r_e)$ in the approaching phase, we have $r_e - 3M \approx \tilde{G}(t_e + D)$ since the first term of the right-hand side of Eq. (88) is approximately zero. This is rewritten as

$$\frac{\delta b}{M} = 2\sqrt{3} \left(\frac{\sqrt{3r_e} - \sqrt{r_e + 6M}}{\sqrt{3r_e} + \sqrt{r_e + 6M}} \right) \exp\left[\frac{t_e + \bar{F}(r_e) - 2C - t_o + F^{(\text{out})}(r_o)}{3\sqrt{3}M}\right], \quad (92)$$

where \bar{F} is defined in Eq. (31). This relation means that a photon traveling from the emission event at (t_e, r_e) to the observation event at (t_o, r_o) must have the impact parameter $b = b_{\text{crit}} + \delta b$ given by this formula. The coordinate values of the observation point (t_o, r_o) appear in Eq. (92) only through the factor $\exp[(-t_o + F^{(\text{out})}(r_o))/3\sqrt{3}M]$. As the observer's time t_o is increased, the required deviation δb from the critical impact parameter becomes exponentially small.

Next, let us consider the case $\delta b < 0$. For this case, we define $G(r)$ as $G(r) := -F^{(\text{in})}(r)$, where $F^{(\text{in})}$ is defined in Eq. (33) with Eqs. (30) and (31). As mentioned in Sec. III B, $t = G(r)$ represents the worldline of a photon with $b = b_{\text{crit}}$ that asymptotes to the photon sphere $r = 3M$ from the inside region. This analytic solution approximates the worldline with $\delta b < 0$ in the approaching phase. Requiring $r - 3M = \tilde{G}(t)$ to be equivalent to $t = G(r)$, we obtain the approximate worldline with $\delta b < 0$ by the same formula as Eq. (88). The behavior of this function in the orbiting phase is given by Eq. (90) with $\sigma = -1$. In order to relate D with δb , we evaluate the value of dr/dt from Eq. (90) at the point where the curve intersects $r = 3M$ and require it to be equal to $dr/dt = (2/27\sqrt{3})^{1/2}(-\delta b/M)^{1/2} + O(\delta b/M)$

evaluated from Eq. (25a) up to the order of $\delta b^{1/2}$. This gives the relation (91). Rewriting Eq. (91), we are led to exactly the same formula for $\delta b/M$ as Eq. (92).

We examine implication of Eq. (92). Since the emission event at (t_e, r_e) is on the world sheet of the star surface given by Eqs. (6b) and (6c) in the parametrized form with respect to ξ , the value of the impact parameter b is determined only by the radius r_e of the star surface at the emission event, or equivalently, the value of ξ for a fixed observation point (t_o, r_o) . In the region $2M < r_e \leq 3\sqrt{3f(R)}M$, δb is a monotonically increasing function of r_e and takes the maximum value b_{limb} at $r_e = 3\sqrt{3f(R)}M$ that corresponds to the limb of the observed image. In the region $3\sqrt{3f(R)}M \leq r_e \leq R$, δb is a monotonically decreasing function of r_e . We do not consider the region $3\sqrt{3f(R)}M \leq r_e \leq R$, because Eqs. (38) and (41) imply that photons with $b \approx b_{\text{crit}}$ emitted from this region have the angle ϑ'_e greater than $\pi/2$ in the comoving frame, which is unrealistic in our setup. Restricting our attention to the region $2M < r_e \leq 3\sqrt{3f(R)}M$, Eq. (92) gives a one-to-one relation between b and r_e .

In order to describe the redshift factor α in this approximation, we use the formula obtained by eliminating $\cos \vartheta_e$ in Eq. (48) through Eq. (38). Here, we set $b = b_{\text{crit}}$ in this relation since our approximation allows the error of $O(\delta b/M)$. This leads to

$$\alpha = \frac{f(r_e)}{\sqrt{f(r_o)f(R)}} \left[1 - \left(1 - \frac{3M}{r_e} \right) \sqrt{\left(1 + \frac{6M}{r_e} \right) \left(1 - \frac{f(r_e)}{f(R)} \right)} \right]^{-1} + O(\delta b/M). \quad (93)$$

Now, for a fixed value of R and the observation point (t_o, r_o) , the redshift factor α is also expressed as a function of r_e . Therefore, we have found the asymptotic relation between δb and α that is parametrically given by r_e .

B. Results

Now, we show the asymptotic behaviors of observable quantities (as already mentioned, we focus on the case $R = 10M$ and $r_o = 50M$). Figure 17 shows the relation between the redshift factor α and the scaled impact parameter $(\delta b/M)e^{(t_o - F^{(\text{out})}(r_o))/3\sqrt{3}M}$. The redshift factor $\alpha(b)$ is a monotonically increasing function. At $b = b_{\text{limb}}$, α takes the value α_{limb} defined in Eq. (50) while the derivative $d\alpha/db$ diverges. If we plot the function $\alpha(b)$ in the (b, α) -plane for large t_o , the curve always passes through the point $(b_{\text{crit}}, \alpha_\infty)$, where α_∞ is defined by Eq. (53), and continues to shrink in the horizontal direction as t_o is increased. This explains the late time behavior of our numerical results of $\alpha(b)$ in Fig. 6.

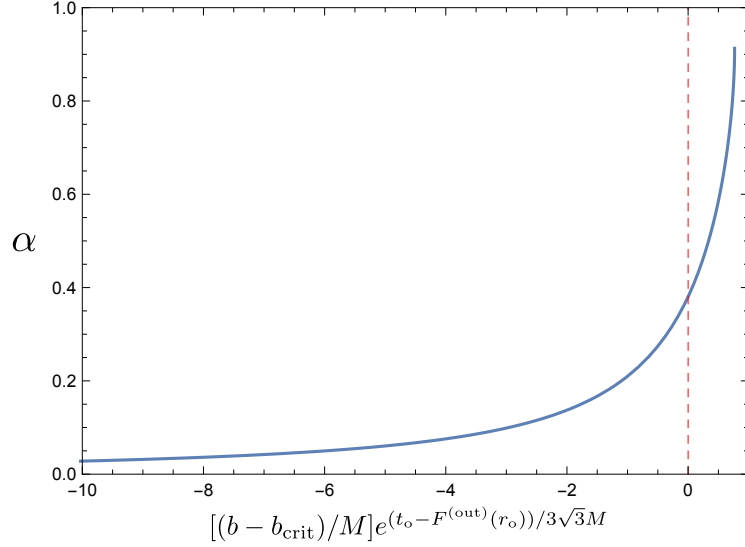


FIG. 17: Asymptotic relation between the (shifted and scaled) impact parameter $[(b - b_{\text{crit}})/M]e^{(t_o - F^{(\text{out})}(r_o))/3\sqrt{3}M}$ and the redshift factor α for $t_o - F^{(\text{out})}(r_o) \gg M$.

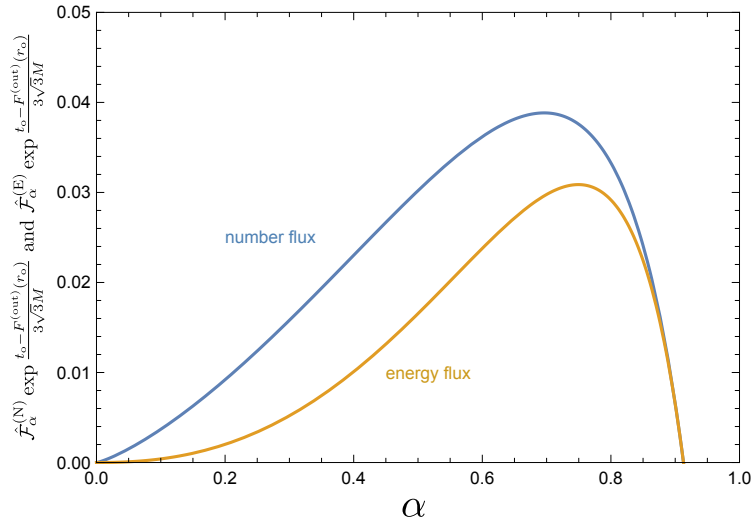


FIG. 18: Asymptotic behavior of the (rescaled) spectral photon/radiant flux for the case of a monochromatic radiator for $t_o - F^{(\text{out})}(r_o) \gg M$. Here, $\hat{\mathcal{F}}_\alpha^{(N)} e^{(t_o - F^{(\text{out})}(r_o))/3\sqrt{3}M}$ and $\hat{\mathcal{F}}_\alpha^{(E)} e^{(t_o - F^{(\text{out})}(r_o))/3\sqrt{3}M}$ are shown as functions of the normalized angular frequency $\alpha := \omega_o/\omega'_e$ (indicated by “number flux” and “energy flux”, respectively).

Now, we show the spectral photon flux and the spectral radiant flux in the monochromatic case given in Eqs. (83a) and (83b). We evaluate only the first terms of these formulas because the second terms vanish for sufficiently large t_o . Since the emission from the star

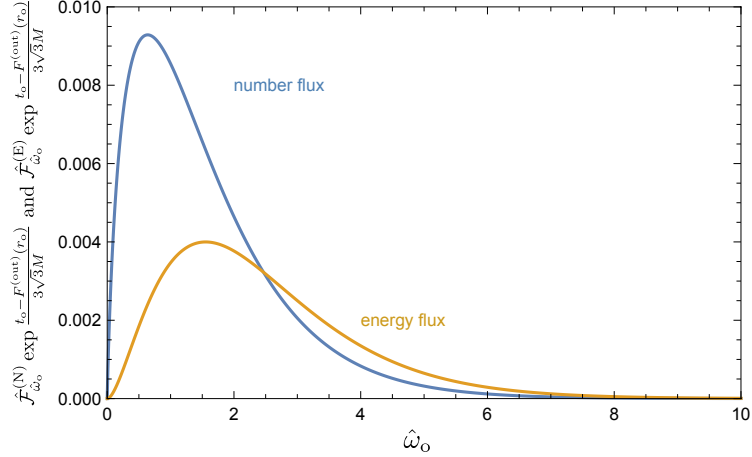


FIG. 19: Same as Fig. 18 but for the case of a blackbody radiator. The horizontal axis is angular frequency normalized by the temperature of the star surface, $\hat{\omega}_o := \omega_o/T'_e$.

surface is assumed to be time independent as assumed in Secs. II B 1 and II B 2, we set $J_e^{(N)}(r_e) = J_e^{(N)}(R)$ and $\langle \omega'_e \rangle|_{r_e} = \langle \omega'_e \rangle|_R$. We approximate these formulas by substituting $b = b_{\text{crit}}$ and calculating $db/d\alpha = [d(\delta b)/dr_e]/(d\alpha/dr_e)$. The quantity dt_e/dr_e , which appears in the calculation of $d(\delta b)/dr_e$, is evaluated using Eqs. (4) and (5). Here, the factor $\exp[(-t_o + F^{(\text{out})}(r_o))/3\sqrt{3}M]$ appears from $d(\delta b)/dr_e$, and thus, the spectral photon/radiant flux decays as the observer's time t_o is increased. Unfortunately, we could not find simple formulas for these quantities, but it is possible to calculate them and plot a figure on *Mathematica*. Figure 18 shows the behavior of the two kinds of rescaled spectral flux, $\hat{\mathcal{F}}_\alpha^{(N)} e^{(t_o - F^{(\text{out})}(r_o))/3\sqrt{3}M}$ and $\hat{\mathcal{F}}_\alpha^{(E)} e^{(t_o - F^{(\text{out})}(r_o))/3\sqrt{3}M}$. They are zero at $\alpha = 0$ and α_{limb} and have peaks at $\alpha \approx 0.696$ and 0.749 , respectively. Integrating $\hat{\mathcal{F}}_\alpha^{(N)}$ with respect to α , it is found that approximately 82% of photons have the redshift factor $\alpha_\infty \leq \alpha \leq \alpha_{\text{limb}}$, and thus, they are emitted while the star radius is within the range $3M \leq r_e \leq 3\sqrt{3f(R)}M$.

Let us discuss the two kinds of spectral flux in the case of a blackbody radiator. We use the formulas (84a) and (84b) with (85), and rewrite $I(\hat{\omega}_o)$ as

$$I(\hat{\omega}_o) \approx \int_{\xi_h}^{\xi_{\text{limb}}} \frac{3\sqrt{3}M}{\exp(\hat{\omega}_o/\alpha) - 1} \left[\frac{d(\delta b)}{dr_e} \right] \left(\frac{dr_e}{d\xi} \right) d\xi, \quad (94)$$

where ξ_h is defined in Eq. (7) and $\xi_{\text{limb}} := 2 \arccos(27M^2 f(R)/R^2)^{1/4}$ is the value of ξ that corresponds to $r_e = 3\sqrt{3f(R)}M$. Here, $d(\delta b)/dr_e$ gives the factor $\exp[(-t_o + F^{(\text{out})}(r_o))/3\sqrt{3}M]$, and thus, $\hat{\mathcal{F}}_{\hat{\omega}_o}^{(N)}$ and $\hat{\mathcal{F}}_{\hat{\omega}_o}^{(E)}$ decay with respect to an observer's time t_o . Although the integral $I(\hat{\omega}_o)$ cannot be proceeded analytically, it is easily integrated numeri-

cally by *Mathematica* because the integrand can be given by an analytic formula. The results for $\hat{\mathcal{F}}_{\hat{\omega}_o}^{(N)} e^{(t_o - F^{(\text{out})}(r_o))/3\sqrt{3}M}$ and $\hat{\mathcal{F}}_{\hat{\omega}_o}^{(E)} e^{(t_o - F^{(\text{out})}(r_o))/3\sqrt{3}M}$ are shown in Fig. 19. The two kinds of spectral flux have peaks at $\hat{\omega}_o = 0.639$ and 1.553 , respectively, resembling Planck's law with a temperature that is about half of that of the star surface.

C. Interpretation

The above derivation of the asymptotic behavior gives a supportive evidence to our numerical results. From the above analysis, the mechanism that causes the asymptotic behavior has become clear. For large t_o , almost all of the observed photons have the impact parameter $b \approx b_{\text{crit}}$, and they arrive at the observer after orbiting in the neighborhood of the photon sphere $r = 3M$. Since most of them are emitted when the radius of the star is within the range $3M \lesssim r_e \leq 3\sqrt{3f(R)}M$, their redshift factor α remains $O(1)$ according to Eq. (93). Therefore, the observed photon intensity (i.e., the observed photon number flux per unit solid angle) is also $O(1)$ around the limb of the star image. But, as an observer's time t_o is increased, the difference of the impact parameter δb of most of the observable photons from the critical one becomes smaller because photons must orbit around $r = 3M$ for a longer time. Due to the relation between b and ϑ_o given by Eq. (38), the bright ring-shaped portion of the star image becomes thinner and thinner, leading to the decay of the total photon number flux. Since the typical scale of δb of arriving photons decays exponentially as $\sim \exp[(-t_o + F^{(\text{out})}(r_o))/3\sqrt{3}M]$ reflecting the instability time scale of the circular orbit, the photon number also decays in the same way.

The discussion here was partly given in Ref. [10]. In that paper, focusing attention to photons that are emitted from the inside region of the photon sphere $r = 3M$ and orbit around the black hole for a long time (class I and II in their definitions), gross features of time evolution of the spectral radiant flux were derived. Our analysis completes their discussion by adding the contribution of backward emitted photons and giving the analytic formulas (92) and (93) for asymptotic behavior for the first time.

VIII. SUMMARY AND DISCUSSION

In this paper, we have studied the propagation of photons from a star under the gravitational collapse and developed a formalism for calculating observable quantities related to photon counting and radiometry. Although this is an old problem, we have revisited this problem taking primary attention to generation of accurate numerical data of the observable quantities. The formulas (67) and (75) for the spectral photon flux and the spectral radiant flux have been derived in the case that the star surface emits radiation that obeys Lambert's cosine law with arbitrary spectral intensity (Sec. IV). After explaining our numerical method in Sec. V, we have applied our formalism to two types of spectra, monochromatic and blackbody radiation, and calculated observable quantities numerically (Sec. VI). There, it has been reconfirmed that at late stage of the collapse, each of the two kinds of spectral flux has a peak at some finite value of angular frequency ω_o : The star becomes invisible not by infinite redshift but by decay of the photon flux. This late time behavior has also been confirmed by an analytic approximate method developed in Sec. VII.

Here, we discuss to what extent our formalism is general. In the setup in Sec. II, we modeled the collapsing star by the Oppenheimer-Snyder solution. But the results of this paper can be applied to arbitrary gravitational collapse where the world sheet of the star surface coincides with a collection of radial timelike geodesics in a Schwarzschild spacetime. Such a situation is realized when pressure of the star is negligible, that is, the Tolman-Bondi collapse [21, 22]. It is known that depending on the initial condition, the Tolman-Bondi collapse leads to the formation of a naked singularity at the center. Our results can be applied to a star under the Tolman-Bondi collapse, as long as nothing is emitted from a naked singularity.

How about the collapse of a star having nonzero pressure? In this case, some of the formulas that uses the speciality of the motion of the star surface, e.g., the third equality in Eq. (39), must be modified. In particular, the constancy of the redshift factor on the limb of the image does not hold for a star surface with nonzero four-acceleration. It would be interesting to extend our formalism to collapses with nonzero pressure, and this issue will be discussed elsewhere. Of course, our method highly depends on the spherical symmetry of the Schwarzschild spacetime. It is an important future problem to extend our formalism to more general cases like axisymmetric collapse of a rotating star.

Does our analysis have a practical meaning for realistic gravitational collapses of stars? As commented in Sec. I, we expect that our analysis would have meaning in the context of neutrino observations rather than electromagnetic observations. Although many simulations have been performed up to now, the mechanism of supernova explosions is still under debate. A very naive expected scenario is as follows. During the collapse, due to the increase in the density of the star, a neutrino-sphere is formed in which neutrinos are trapped. The core bounce happens due to the formation of a proto-neutron star, and a shock propagates toward outward direction. In the case that the supernova explosion happens, the shock stalls during the propagation, but it revives by some mechanisms (including reheating by neutrinos) and blows the star surface off. The proto-neutron star at the center gradually cools down and becomes a neutron star. By contrast, if the star fails to explode, which is called a failed supernova, matter of the star continues to be accreted onto the proto-neutron star. As a result, the proto-neutron star is expected to begin gravitational collapse and become a black hole. In this case, the neutrino sphere would fall into the black hole as well. In Refs. [23–25], it was argued that if the neutrino flux is measurably high in this stage, the neutrino flux would be terminated abruptly. Our study in this paper is a necessary step toward predicting the detailed process of this neutrino flux truncation including general relativistic effects on neutrino propagation.

Another interesting direction is the multimessenger observations. In Refs. [26, 27], gravitational waves generated by contracting magnetic fields during the Oppenheimer-Snyder collapse were studied by treating both electromagnetic fields and gravitational waves as perturbations. Simultaneous observations of gravitational waves and neutrinos would give more information on a collapsing star under strong gravity environment.

The most fascinating possibility is the black hole formation in the gravitational collapse of Betelgeuse, which is a red giant nearing the end of its life. Its distance from the Earth is estimated as 197 ± 45 pc [28], and if a failed supernova happens at such a close position, observations will give us various valuable information including general relativistic effects near the black hole. The study of this paper is a necessary step to prepare for such a possibility.

Acknowledgments

We thank Yudai Suwa, Takaaki Kajita, Tomohiro Harada, Hirotada Okawa and Hajime Sotani for helpful comments. We also thank the International Molecule-type Workshop “Dynamics in Strong Gravity Universe” (YITP-T-18-05) held at Yukawa Institute for Theoretical Physics at Kyoto University for hospitality. The work of H.Y. was supported by the Grant-in-Aid for Scientific Research (C) (Grant No. JP18K03654) from Japan Society for the Promotion of Science (JSPS). This work was partly supported by Osaka City University Advanced Mathematical Institute (MEXT Joint Usage/Research Center on Mathematics and Theoretical Physics).

Appendix A: Approximate analysis near the center of the image

In this appendix, we study perturbative approximation around the center of the disk image. To be specific, the redshift factor $\alpha(b)$ is studied for small b values (i.e., small ϑ_o values) by a perturbative method, and the two kinds of spectral flux, $\hat{\mathcal{F}}_\alpha^{(N)}$ and $\hat{\mathcal{F}}_\alpha^{(E)}$, defined in Eqs. (83a) and (83b) in the neighborhood of the central value of the redshift factor are studied for a monochromatic radiator. The late time behavior of these quantities is also presented.

1. The redshift factor

From Eq. (48), varying b from zero causes the change in the redshift factor through the two effects: The change in the emitted angle ϑ_e and the change in the radius r_e at the emission event. Because the first effect can be absorbed into the second effect by the relation (38), we begin with examining the dependence of the radius r_e on b . By perturbative expansion with respect to b^2 , the geodesic equation for photons, Eq. (25a), with the plus sign becomes

$$\frac{dt}{dr} = f^{-1} + \frac{b^2}{2r^2} + \frac{3b^4}{8r^4}f + O(b^6). \quad (\text{A1})$$

Integrating this equation and substituting $(t, r) = (t_e(r_e), r_e)$, we have

$$\begin{aligned} t_e(r_e) - t_o = r_e - r_o + 2M \log \left(\frac{r_e - 2M}{r_o - 2M} \right) - \frac{b^2}{2} \left(\frac{1}{r_e} - \frac{1}{r_o} \right) \\ + b^4 \left[-\frac{1}{8} \left(\frac{1}{r_e^3} - \frac{1}{r_o^3} \right) + \frac{3M}{16} \left(\frac{1}{r_e^4} - \frac{1}{r_o^4} \right) \right] + O(b^6) \end{aligned} \quad (\text{A2})$$

We give the expansion form of r_e as

$$r_e(b) = r_e^{(0)} + r_e^{(1)}b^2 + r_e^{(2)}b^4 + O(b^6), \quad (\text{A3})$$

where $r_e^{(n)}$ denotes the n -th order quantity with respect to the small parameter b^2 . Here, the zeroth-order quantity $r_e^{(0)}$ satisfies

$$t_o = t_e(r_e^{(0)}) - r_e^{(0)} + r_o - 2M \log \left(\frac{r_e^{(0)} - 2M}{r_o - 2M} \right). \quad (\text{A4})$$

From this formula, together with Eqs. (6b) and (6c), t_o is expressed as a function of $r_e^{(0)}$. We substitute Eq. (A3) into Eq. (A2) and collect terms with the same order. In expanding $t_e(r_e)$, the quantities $dt_e/dr_e|_{r_e=r_e^{(0)}}$ and $d^2t_e/dr_e^2|_{r_e=r_e^{(0)}}$ appear, and we use Eqs. (4) and (5) in order to evaluate these quantities. As a result, we find

$$r_e^{(1)} = \frac{(1/2)f}{1 + (1 - f/f(R))^{-1/2}} \left(\frac{1}{r_e^{(0)}} - \frac{1}{r_o} \right), \quad (\text{A5})$$

$$r_e^{(2)} = \frac{f}{1 + (1 - f/f(R))^{-1/2}} \left\{ \frac{f'}{4f^2} \left[2 + \frac{2 - 3f/f(R)}{(1 - f/f(R))^{3/2}} \right] r_e^{(1)2} - \frac{r_e^{(1)}}{2r_e^{(0)2}} + \frac{1}{8} \left(\frac{1}{r_e^{(0)3}} - \frac{1}{r_o^3} \right) - \frac{3M}{16} \left(\frac{1}{r_e^{(0)4}} - \frac{1}{r_o^4} \right) \right\}, \quad (\text{A6})$$

where f and f' are evaluated at $r_e^{(0)}$. Since $r_e(b)$ is also expressed in terms of $r_e^{(0)}$, we have obtained the relation between $r_e(b)$ and t_o .

Now, we examine the expansion formula of α . For small values of b^2 , the redshift factor α is given by

$$\alpha = \frac{f(r_e)}{\sqrt{f(r_o)f(R)}} \left[1 + \sqrt{\left(1 - \frac{f(r_e)}{f(R)} \right) \left(1 - \frac{f(r_e)}{r_e^2} b^2 \right)} \right]^{-1} \quad (\text{A7})$$

from Eqs. (38) and (48). Substituting Eq. (A3) and expanding with respect to b , we find the expansion form,

$$\alpha = \alpha^{(0)} + \alpha^{(1)}b^2 + \alpha^{(2)}b^4 + O(b^6), \quad (\text{A8})$$

where $\alpha^{(n)}$ denotes the n -th order term with respect to the expansion parameter b^2 . Here, $\alpha^{(0)}$ coincides with the value at the center of the image, α_{cent} in the main article, and it is

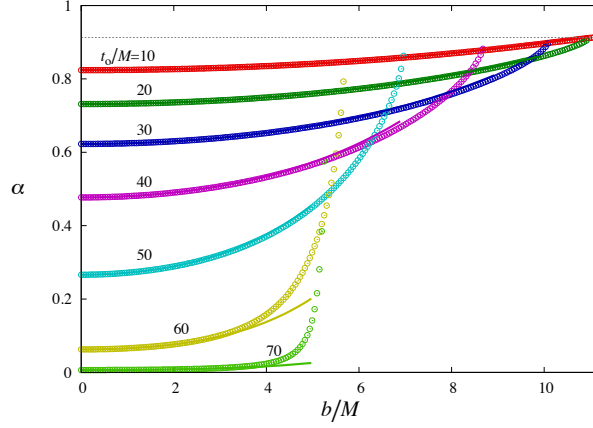


FIG. 20: The behavior of the redshift factor α as a function of b near the center $b = 0$ obtained by the approximate formula (A8) (solid curves) and the numerical data (circles, \circ). The data are shown for the observer's time $t_o/M = 10, 20, \dots, 70$ in the case $R = 10M$ and $r_o = 50M$.

trivially obtained by substituting $r_e = r_e^{(0)}$ and $b = 0$ into Eq. (A7). $\alpha^{(1)}$ is calculated as

$$\alpha^{(1)} = \frac{f}{2\sqrt{f(r_o)f(R)} r_e^{(0)2}} \left[1 + \sqrt{1 - \frac{f}{f(R)}} \right]^{-2} \times \left[\frac{M}{r_e^{(0)}} - \frac{M}{r_o} + \sqrt{1 - \frac{f}{f(R)}} \left(1 - \frac{M}{r_e^{(0)}} - \frac{M}{r_o} \right) \right]. \quad (\text{A9})$$

Although we do not present the complicated form of $\alpha^{(2)}$ here, it is easily calculated by, e.g., *Mathematica*. Figure 20 shows the behavior of the approximate formula (A8) of $\alpha(b)$ for $t_o/M = 10, \dots, 70$ in the case $R = 10M$ and $r_o = 50M$. For $t_o \lesssim 10M$, this formula approximately coincides with the numerical data of $\alpha(b)$ in a fairly large domain of b (up to $b \lesssim 10M$). Although such domain becomes smaller as the observer's time is increased, the numerical data agree well with the approximate formula for $b \lesssim 2M$.

2. Spectral flux for a monochromatic radiator

In the case of a monochromatic radiator, the spectral photon/radiant flux is zero in the range $0 \leq \alpha < \alpha^{(0)}$ and has nonzero values for $\alpha^{(0)} \leq \alpha \leq \alpha_{\text{limb}}$. In the nonzero region, the two kinds of spectral flux are given by the first terms of the formulas (83a) and (83b) with $J_e^{(N)}(r_e) = J_e^{(N)}(R)$ and $\langle \omega'_e \rangle|_{r_e} = \langle \omega'_e \rangle|_R$. Substituting the expansion formula for α , they are

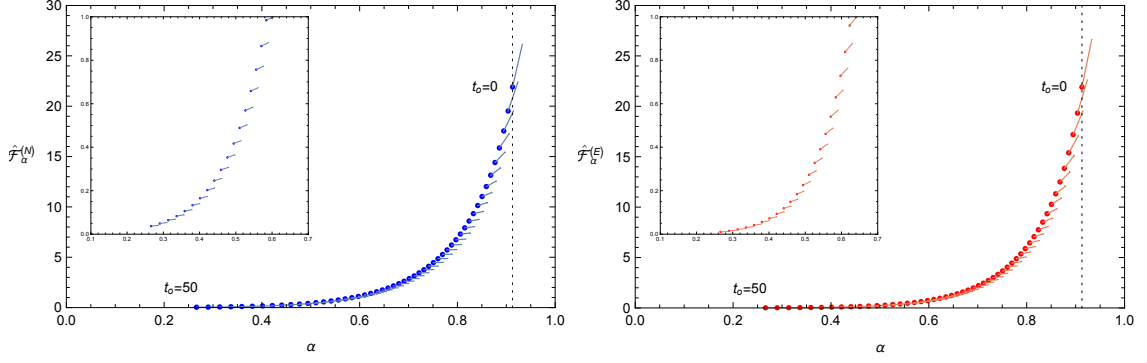


FIG. 21: The behavior of $\hat{\mathcal{F}}_\alpha^{(N)}$ (left panel) and $\hat{\mathcal{F}}_\alpha^{(E)}$ (right panel) in the neighborhood of $\alpha = \alpha^{(0)}$ obtained by the approximate formulas (A10a) and (A10b) for $t_o = 0, 1, \dots, 50$ (in the unit $M = 1$). Inset of each panel enlarges the late time data.

rewritten as

$$\hat{\mathcal{F}}_\alpha^{(N)} \approx \frac{f(r_o)^{3/2}}{R^2 f(R)^{1/2}} \frac{\alpha^{(0)3}}{\alpha^{(1)}} \left[1 + \frac{1}{\alpha^{(1)}} \left(\frac{3\alpha^{(1)}}{\alpha^{(0)}} - \frac{2\alpha^{(2)}}{\alpha^{(1)}} \right) (\alpha - \alpha^{(0)}) \right], \quad (\text{A10a})$$

$$\hat{\mathcal{F}}_\alpha^{(E)} \approx \frac{f(r_o)^2}{R^2 f(R)} \frac{\alpha^{(0)4}}{\alpha^{(1)}} \left[1 + \frac{2}{\alpha^{(1)}} \left(\frac{2\alpha^{(1)}}{\alpha^{(0)}} - \frac{\alpha^{(2)}}{\alpha^{(1)}} \right) (\alpha - \alpha^{(0)}) \right], \quad (\text{A10b})$$

in the neighborhood of $\alpha = \alpha^{(0)}$. Figure 21 shows the behavior of $\hat{\mathcal{F}}_\alpha^{(N)}$ (left panel) and $\hat{\mathcal{F}}_\alpha^{(E)}$ (right panel) in the neighborhood of $\alpha = \alpha^{(0)}$ obtained by these formulas for $t_o = 0, 1, \dots, 50$ (in the unit $M = 1$).

3. Late time behavior of observable quantities

We study late time behavior of the redshift factor $\alpha^{(0)}$ at the central point and the two kinds of normalized spectral flux, $\hat{\mathcal{F}}_\alpha^{(N)}$ and $\hat{\mathcal{F}}_\alpha^{(E)}$, at $\alpha = \alpha^{(0)}$. Since photons that come to the center of the disk image are emitted from the near horizon region $r \approx 2M$, we keep only leading order terms of $(r_e^{(0)} - 2M)$ in this approximation. The world sheet (6b) and (6c) of the star surface is approximately given by

$$t_e + \mathcal{T} \approx 2M \log \left[\frac{4f(R)}{f(r_e)} \right] + 4MC', \quad (\text{A11})$$

with

$$C' := \left(\frac{R}{2M} - 1 \right) + \frac{\xi_h}{2} \sqrt{\frac{R}{2M} - 1} \left(1 + \frac{R}{4M} \right), \quad (\text{A12})$$

where \mathcal{T} and ξ_h are defined in Eqs. (20) and (7), respectively. Substituting $r_e = r_e^{(0)}$ into this formula and combining with the relation (A4), we have

$$f(r_e^{(0)}) \approx \sqrt{\frac{2R}{M}} f(R) e^{C'} e^{-t_o/4M}. \quad (\text{A13})$$

Since $\alpha^{(0)}$ and $\alpha^{(1)}$ are approximated as

$$\alpha^{(0)} \approx \frac{f(r_e^{(0)})}{2\sqrt{f(r_o)f(R)}} \quad \text{and} \quad \alpha^{(1)} \approx \sqrt{\frac{f(r_o)}{f(R)}} \frac{f(r_e^{(0)})}{32M^2}, \quad (\text{A14})$$

respectively, we obtain the late time behavior for the redshift factor,

$$\alpha^{(0)} \approx \sqrt{\frac{Rf(R)}{2Mf(r_o)}} e^{C'} e^{-t_o/4M}, \quad (\text{A15})$$

and the two kinds of spectral flux,

$$\hat{\mathcal{F}}_\alpha^{(N)} \Big|_{\alpha^{(0)}} \approx \frac{8M}{R} \sqrt{\frac{f(R)}{f(r_o)}} e^{2C'} e^{-t_o/2M}, \quad (\text{A16a})$$

$$\hat{\mathcal{F}}_\alpha^{(E)} \Big|_{\alpha^{(0)}} \approx 4 \sqrt{\frac{2Mf(R)}{Rf(r_o)}} e^{3C'} e^{-3t_o/4M}. \quad (\text{A16b})$$

at the central point $b = 0$ (i.e., $\vartheta_o = 0$).

-
- [1] B. P. Abbott *et al.* (LIGO Scientific and Virgo Collaborations), Phys. Rev. Lett. **116**, 061102 (2016) [arXiv:1602.03837 [gr-qc]].
 - [2] K. Akiyama *et al.* (Event Horizon Telescope Collaboration), Astrophys. J. **875**, L1 (2019) [arXiv:1906.11238 [astro-ph.GA]].
 - [3] C. Bambi, K. Freese, S. Vagnozzi, and L. Visinelli, Phys. Rev. D **100**, 044057 (2019) [arXiv:1904.12983 [gr-qc]].
 - [4] K. S. Virbhadra and G. F. R. Ellis, Phys. Rev. D **62**, 084003 (2000) [astro-ph/9904193].
 - [5] C. M. Claudel, K. S. Virbhadra and G. F. R. Ellis, J. Math. Phys. (N.Y.) **42**, 818 (2001) [gr-qc/0005050].
 - [6] P. V. P. Cunha, C. A. R. Herdeiro, and E. Radu, Phys. Rev. D **96**, 024039 (2017) [arXiv:1705.05461 [gr-qc]].
 - [7] V. Cardoso and P. Pani, Nat. Astron. **1**, 586 (2017) [arXiv:1707.03021 [gr-qc]].

- [8] J. R. Oppenheimer and H. Snyder, Phys. Rev. **56**, 455 (1939).
- [9] M. A. Podurets, Sov. Astron. A. J. **8**, 868 (1965).
- [10] W. L. Ames and K. Thorne, Astrophys. J. **151**, 659 (1968).
- [11] J. Jaffe, Ann. Phys. (N.Y.) **55**, 374 (1969).
- [12] K. Lake and R. C. Roeder, Astrophys. J. **232**, 277 (1979).
- [13] C. W. Misner, K. S. Thorne, and J. A. Wheeler, *Gravitation* (W. H. Freeman and Company, New York, 1973).
- [14] S. L. Shapiro, Phys. Rev. D **40**, 1858 (1989).
- [15] S. L. Shapiro, Astrophys. J. **472**, 308 (1996).
- [16] V. P. Frolov and H. K. Lee, Phys. Rev. D **71**, 044002 (2005) [gr-qc/0412124].
- [17] V. P. Frolov, K. Kim and H. K. Lee, Phys. Rev. D **75**, 087501 (2007) [gr-qc/0701001].
- [18] K. Abe *et al.*, Nucl. Instrum. Methods Phys. Res., Sect. A **737**, 253 (2014) [arXiv:1307.0162 [physics.ins-det]].
- [19] P. E. J. Schneider and E. E. Falco, *Gravitational Lenses* (Springer, New York, 1992).
- [20] I. M. H. Etherington, Philos. Mag. **15** (1933).
- [21] R. C. Tolman, Proc. Natl. Acad. Sci. U.S.A. **20**, 410 (1934).
- [22] H. Bondi, Mon. Not. Astron. Soc. **107**, 343 (1947).
- [23] T. W. Baumgarte, S. A. Teukolsky, S. L. Shapiro, H. T. Janka and W. Keil, Astrophys. J. **468**, 823 (1996).
- [24] J. F. Beacom, R. N. Boyd, and A. Mezzacappa, Phys. Rev. D **63**, 073011 (2001) [astro-ph/0010398].
- [25] T. Sasaqui, T. Kajino, and A. B. Balantekin, Astrophys. J. **634**, 534 (2005) [astro-ph/0506100].
- [26] H. Sotani, S. Yoshida and K. D. Kokkotas, Phys. Rev. D **75**, 084015 (2007) [gr-qc/0702091].
- [27] H. Sotani, Phys. Rev. D **79**, 084037 (2009) [arXiv:0904.1465 [gr-qc]].
- [28] G. M. Harper, A. Brown, and E. F. Guinan, Astronom. J. **135**, 1430 (2008).